Lipid signalling enforces T$_{reg}$ cell functional specialization in tumours

Seon Ah Lim[1,*], **Jun Wei**[1,*], **Thanh-Long M. Nguyen**[1], **Hao Shi**[1], **Wei Su**[1], **Gustavo Palacios**[1], **Yogesh Dhungana**[1], **Nicole M. Chapman**[1], **Lingyun Long**[1], **Jordy Saravia**[1], **Peter Vogel**[2], **Hongbo Chi**[1]

[1]Department of Immunology, St. Jude Children's Research Hospital, Memphis, TN 38105, USA.

[2]Department of Pathology, St. Jude Children's Research Hospital, Memphis, TN 38105, USA.

Abstract

Regulatory T (T$_{reg}$) cells are essential for immune tolerance1 but also drive immunosuppression in the tumour microenvironment (TME)2. Therapeutic targeting of T$_{reg}$ cells in cancer requires the identification of context-specific mechanisms for T$_{reg}$ cell function. Here we demonstrate that inhibition of sterol regulatory element-binding protein (SREBP)-dependent lipid synthesis and metabolic signalling in T$_{reg}$ cells unleashes effective antitumour immune responses without autoimmune toxicity. SREBP activity is upregulated in intratumoural T$_{reg}$ cells, and T$_{reg}$ cell-specific deletion of SCAP, an obligatory factor for SREBP activity, inhibits tumour growth and boosts anti-PD-1 immunotherapy, associated with uncontrolled IFN-γ production and impaired function of intratumoural T$_{reg}$ cells. Mechanistically, SCAP/SREBP signalling coordinates lipid synthetic programs and inhibitory receptor signalling in T$_{reg}$ cells. First, *de novo* fatty acid synthesis mediated by fatty acid synthase (FASN) contributes to functional maturation of T$_{reg}$ cells, and loss of FASN in T$_{reg}$ cells inhibits tumour growth. Second, T$_{reg}$ cells show enhanced *Pdcd1* expression in tumours in a process dependent on SREBP activity that further signals to mevalonate metabolism-driven protein geranylgeranylation, and blocking PD-1 or SREBP signaling results in dysregulated PI3K activation in intratumoural T$_{reg}$ cells. Our findings establish that metabolic reprogramming enforces T$_{reg}$ cell functional specialization in tumours, pointing to new avenues to target T$_{reg}$ cells for cancer therapy.

Emerging studies reveal the critical roles of immunometabolism in regulating cell state and fate[3,4], but context-dependent metabolic effects *in vivo* are underexplored. In particular, how

Correspondence should be addressed to: **Hongbo Chi**, Department of Immunology, St. Jude Children's Research Hospital, Memphis, TN 38105, USA. Phone: 901-595-6282; Fax: 901-595-5766; hongbo.chi@stjude.org.
*These authors contributed equally to this work.

T_{reg} cells rewire metabolic programs to enforce functional adaptation in tumours remains unclear, despite the identification of metabolic pathways supporting T_{reg} cell function under homeostasis[4,5]. To explore the molecular basis for T_{reg} cell functional adaptation in tumours, we performed transcriptome analysis of T_{reg} cells isolated from tumour and peripheral tissues after challenging wild-type (WT) mice with B16 melanoma cells. Gene set enrichment analysis (GSEA) using curated metabolic pathways (Supplementary Table 1) revealed that lipid metabolism-related pathways were among the top enriched pathways in intratumoural T_{reg} cells compared to those from peripheral lymph nodes (PLNs) (Fig. 1a). In particular, gene targets for transcription factors SREBPs, which promote *de novo* synthesis of lipids including fatty acids and cholesterol (Extended Data Fig. 1a)[6], were the most enriched gene signature (Fig. 1a and Extended Data Fig. 1b). Ingenuity pathway analysis also revealed that SREBP1 (encoded by *Srebf1*) and SREBP2 (*Srebf2*) were among the top enriched upstream transcriptional regulators in intratumoural T_{reg} cells (Extended Data Fig. 1c). Such enrichment was further validated in public single-cell RNA sequencing (scRNA-seq) datasets of mouse melanoma models[7,8] (Extended Data Fig. 1d, e) and human patients with breast cancer[9] (Extended Data Fig. 1f) or head and neck squamous cell carcinoma[10] (Extended Data Fig. 1g), indicating upregulation of the SREBP gene signature in T_{reg} cells from the TME.

We next explored whether SREBP signalling in T_{reg} cells is affected by other inflammatory signals. We first analyzed a public transcriptome dataset of activated T_{reg} (aT_{reg}) cells in an acute inflammation model[11], and found that SREBP gene targets were not enriched in aT_{reg} cells compared to resting T_{reg} (rT_{reg}) cells (Extended Data Fig. 1h). scRNA-seq analysis of T_{reg} cells from the CNS of experimental autoimmune encephalomyelitis (EAE) mice also did not show increased SREBP gene targets (Extended Data Fig. 1i, j). By contrast, although glucose metabolism supports T_{reg} cell proliferation and survival in tumours[12], intratumoural T_{reg} cells did not increase glucose uptake compared with splenic counterparts (Extended Data Fig. 1k). Instead, glucose uptake was upregulated in T_{reg} cells from EAE mice (Extended Data Fig. 1l). These results reveal context-specific adaptation of SREBP signature in T_{reg} cells from the TME.

To determine the functional importance of SREBP signalling in T_{reg} cells, we crossed mice with *lox*P-flanked *Scap* alleles with *Foxp3*[YFP-Cre] mice (*Foxp3*[Cre]*Scap*^{fl/fl}) to delete *Scap* specifically in T_{reg} cells (Extended Data Fig. 1m). Deletion of SCAP inhibited expression of SREBP gene targets in intratumoural T_{reg} cells (Extended Data Fig. 1n). We next challenged *Foxp3*[Cre]*Scap*^{fl/fl} mice with models of MC38 colon adenocarcinoma and B16 melanoma. While MC38 colon adenocarcinoma had progressive growth in control mice, *Foxp3*[Cre]*Scap*^{fl/fl} mice showed a rapid and complete clearance of tumour cells (Fig. 1b). Additionally, the growth of B16 melanoma was significantly reduced in *Foxp3*[Cre]*Scap*^{fl/fl} mice (Fig. 1c). To explore the potential of targeting SCAP/SREBP signalling for the treatment of established tumours, we generated *Foxp3*[GFP-Cre-ERT2]*Scap*^{fl/fl}*Rosa26*[YFP] mice to acutely delete *Scap* in T_{reg} cells upon tamoxifen treatment[13,14] when the tumour started to appear or was fully established. Under both treatment regimens, tumour growth was reduced in *Foxp3*[GFP-Cre-ERT2]*Scap*^{fl/fl}*Rosa26*[YFP] mice (Fig. 1d, e), while no difference in tumour growth was found without tamoxifen treatment (Extended Data Fig. 1o). We next explored the combinatorial effect of T_{reg} cell-specific SCAP deletion with anti-PD-1 immunotherapy.

While B16 melanoma growth was largely refractory to anti-PD-1 therapy[15], deletion of SCAP in T_{reg} cells sensitized the mice to anti-PD-1 therapy (Fig. 1f). These results from various models indicate that targeting SCAP/SREBP signalling in T_{reg} cells unleashes potent antitumour effects.

T_{reg} cells are essential in maintaining immune homeostasis[1]. Compared to control mice, *Foxp3*^{Cre}*Scap*$^{fl/fl}$ mice had normal cellularity and effector/memory population (CD44^{hi}CD62L^{lo}) of Foxp3$^-$CD4$^+$ and CD8$^+$ T cells in the spleen and PLNs (Extended Data Fig. 2a, b), as well as inflammatory cytokine production (Extended Data Fig. 2c, d). Accordingly, *Foxp3*^{Cre}*Scap*$^{fl/fl}$ mice did not show histological abnormality in multiple organs examined, except for minor inflammation in the pancreas (Extended Data Fig. 2e). Also, serum anti-nuclear and anti-dsDNA antibodies were not elevated (Extended Data Fig. 2f, g), and life span was normal (Extended Data Fig. 2h). Thus, SCAP activity is largely dispensable for supporting T_{reg} cell function in maintaining self-tolerance under steady state.

Moreover, upon induction of EAE disease, *Foxp3*^{Cre}*Scap*$^{fl/fl}$ mice had no alterations in disease scores (Extended Data Fig. 3a), CNS inflammation (Extended Data Fig. 3b), or T cell infiltration and cytokine production (Extended Data Fig. 3c, d). Additionally, we generated female *Foxp3*$^{Cre/DTR}$*Scap*$^{fl/fl}$ or control mosaic mice to target the *Foxp3* gene that resides in the X-chromosome, with acute depletion of DTR-expressing T_{reg} cells with DT driving the activation of the remaining SCAP-deficient or control T_{reg} cells to enforce immunosuppression[16,17]. In this model of acute inflammation, *Foxp3*$^{Cre/DTR}$*Scap*$^{fl/fl}$ mice showed normal cellularity, activation and cytokine production of Foxp3$^-$CD4$^+$ and CD8$^+$ T cells (Extended Data Fig. 3e–h), suggesting the normal suppressive function of SCAP-deficient T_{reg} cells. Altogether, loss of SCAP/SREBP signalling in T_{reg} cells suppresses tumour growth without discernable autoimmune or inflammatory consequences.

To determine the effects of SCAP-deficient T_{reg} cells at shaping the TME, we used scRNA-seq to unbiasedly profile CD45$^+$ immune cells in B16 tumour-bearing mice (Fig. 2a). Compared with control mice, there were increased proportions of total and effector/memory-phenotype CD8$^+$ T cells and total Foxp3$^-$CD4$^+$ T cells in the TME from *Foxp3*^{Cre}*Scap*$^{fl/fl}$ mice (Fig. 2b), which was verified by flow cytometry analysis (Extended Data Fig. 4a, b), including the increased numbers of CD8$^+$ T cells with effector (CD44^{hi}CD62L^{lo}; T_{eff}) and central memory (CD44^{hi}CD62L^{hi}; T_{cm}) but not exhaustion (Tim3$^+$PD-1$^+$; T_{ex}) phenotypes (Extended Data Fig. 4c–e). There was also an increase in the frequency of TNF-α$^+$ (and trending increase in IFN-γ$^+$) CD8$^+$ and Foxp3$^-$CD4$^+$ T cells from tumours but not PLNs (Extended Data Fig. 4f, g). The ratio of CD8$^+$ T cells versus T_{reg} cells, a critical prognostic factor for cancer[2], was also increased in *Foxp3*^{Cre}*Scap*$^{fl/fl}$ tumours (Fig. 2c). Moreover, while MC38 colon adenocarcinoma was rejected in *Foxp3*^{Cre}*Scap*$^{fl/fl}$ mice (Fig. 1b), depletion of CD8$^+$ T cells partially restored tumour growth (Extended Data Fig. 4h), indicating the partial dependence on CD8$^+$ T cell responses for these effects.

Further, scRNA-seq analysis identified a reduced proportion of T_{reg} cells in tumours from *Foxp3*^{Cre}*Scap*$^{fl/fl}$ mice (Fig. 2b). Flow cytometry analysis also revealed a reduced T_{reg} cell frequency in tumours but not PLNs from *Foxp3*^{Cre}*Scap*$^{fl/fl}$ mice (Extended Data Fig. 5a), whereas the number of intratumoural T_{reg} cell was not reduced (Extended Data Fig. 5a),

likely because of the increase in total tumour-infiltrating lymphocytes (Extended Data Fig. 5b). In contrast to tumours, there were no changes in T_{reg} cell accumulation under steady state (Extended Data Fig. 5c). We next examined the effects of SCAP deficiency on T_{reg} cell state. Consistent with the requirement of SCAP-mediated cholesterol biosynthesis for $CD8^+$ T cell proliferation upon acute antigen stimulation[18], SCAP-deficient T_{reg} cells had defective proliferation *in vitro*, which was partially reversed by cholesterol supplementation (Extended Data Fig. 5d). However, T_{reg} cells in tumours or PLNs from *Foxp3*[Cre]*Scap*^{fl/fl} mice did not exhibit altered BrdU incorporation (Extended Data Fig. 5e), and SCAP-deficient peripheral T_{reg} cells also had normal lymphopenia-induced proliferation (Extended Data Fig. 5f) and IL-2/anti-IL-2 complex-induced expansion[19,20] (Extended Data Fig. 5g). Additionally, expression of CTLA4, which is closely associated with metabolism-driven proliferation[21], was not altered by SCAP deficiency (Extended Data Fig. 5h, i). Therefore, SCAP function is largely dispensable for T_{reg} cell proliferation under homeostasis and in the TME, highlighting a context-specific proliferative requirement as observed in $CD8^+$ T cells[18]. Next, we examined T_{reg} cell apoptosis and found that SCAP-deficient T_{reg} cells had increased staining of active caspase-3 in tumours but not PLNs (Extended Data Fig. 5j). The elevated cell death due to SCAP deficiency was also observed in a cell-intrinsic system of female *Foxp3*[Cre/+]*Scap*^{fl/fl} mosaic mice that contained *Scap*-deficient and -sufficient T_{reg} cells[19], associated with reduced frequency and trending numerical reduction of intratumoural T_{reg} cells (Extended Data Fig. 5k–m). However, expression of CD36, which mediates lipid uptake for intratumoural T_{reg} cell survival[22], as well as neutral lipid uptake, were unaffected by SCAP deficiency (Extended Data Fig. 5n, o). Control and SCAP-deficient T_{reg} cells also showed comparable mitochondrial profiles, including mitochondrial mass, membrane potential, and reactive oxygen species production (Extended Data Fig. 5p). Thus, SCAP is dispensable for lipid uptake or mitochondrial fitness but contributes to intratumoural T_{reg} cell survival.

We next examined the possible involvement of SCAP for the differentiation of T_{reg} cells from quiescent rT_{reg} ($CD44^{lo}CD62L^{hi}$) into aT_{reg} ($CD44^{hi}CD62L^{lo}$) population[1,23], and the maintenance of Foxp3 expression[1], both of which are shaped by inflammatory conditions. Under steady state, aT_{reg} cell accumulation was unchanged in the absence of SCAP (Extended Data Fig. 5q). Also, intratumoural SCAP-deficient T_{reg} cells contained a normal percentage and number of the aT_{reg} cell subset (Extended Data Fig. 5r). Moreover, Foxp3 expression was comparable in control and SCAP-deficient intratumoural T_{reg} cells (Extended Data Fig. 6a, b), as well as in T_{reg} cells upon transfer into *Rag1*^{−/−} mice[24] (Extended Data Fig. 6c). These results indicate a dispensable role of SCAP for aT_{reg} cell accumulation and Foxp3 expression.

Intratumoural T_{reg} cells can become fragile, a unique cellular state marked by retention of Foxp3 expression but aberrant IFN-γ production[25,26]. While IFN-γ-expressing T_{reg} cells were unaltered by SCAP deficiency at steady state (Extended Data Fig. 6d), there was an increased frequency of IFN-γ^+ T_{reg} cells in tumours but not PLNs from *Foxp3*[Cre]*Scap*^{fl/fl} mice than controls (Fig. 2d). scRNA-seq analysis also revealed that macrophages in tumours from *Foxp3*[Cre]*Scap*^{fl/fl} mice had elevated expression of IFN-γ-inducible imunomodulatory genes *B2m*, *H2-Aa* and *Cd274*[27] (Extended Data Fig. 6e). Moreover, the growth of both B16 melanoma and MC38 colon adenocarcinoma was substantially inhibited in female

$Foxp3^{Cre/+}Scap^{fl/fl}$ mosaic mice (Fig. 2e, f), in line with the dominant effect of fragile T_{reg} cells at reshaping the TME[25,26]. Furthermore, in the aforementioned tamoxifen-inducible system (Fig. 1d), both SCAP-deficient and -sufficient T_{reg} cells showed a trending increase of IFN-γ^+ T_{reg} cell frequency in tumours but not PLNs from $Foxp3^{GFP\text{-}Cre\text{-}ERT2}Scap^{fl/fl}Rosa26^{YFP}$ mice (Extended Data Fig. 6f), associated with significantly increased frequencies of IFN-γ^+ and TNF-α^+ CD8$^+$ and Foxp3$^-$CD4$^+$ T cells (Extended Data Fig. 6g, h). Altogether, SCAP/SREBP signalling is critical for maintaining the functional integrity of T_{reg} cells in the TME.

In transcriptome analysis of tumour-infiltrating T_{reg} cells from control and $Foxp3^{Cre}Scap^{fl/fl}$ mice, GSEA revealed that the hallmark pathways of cholesterol homeostasis and fatty acid metabolism were among the top-ranking downregulated gene sets in SCAP-deficient T_{reg} cells (Fig. 3a, b), along with reduced expression of $Hmgcr$ and $Fasn$ (Extended Data Fig. 1n) that encode HMG-CoA reductase and fatty acid synthase to drive mevalonate and fatty acid biosynthesis pathways, respectively[6]. While T_{reg} cell-specific deletion of $Hmgcr$ leads to a $Scurfy$-like autoimmune phenotype[28], partial loss of $Hmgcr$ expression, as observed in T_{reg} cells from $Foxp3^{Cre}Scap^{fl/fl}$ or $Foxp3^{Cre}Hmgcr^{+/fl}$ mice (Extended Data Fig. 7a, b), did not alter immune homeostasis (Extended Data Fig. 7c). Moreover, T_{reg} cell-specific deletion of FASN ($Foxp3^{Cre}Fasn^{fl/fl}$; Extended Data Fig. 7d) did not alter cellularity of Foxp3$^+$ T_{reg} or conventional T cells (Extended Data Fig. 7e, f), or the activation state and cytokine production (Extended Data Fig. 7g–i). These results indicate a dispensable role of fatty acid synthesis for T_{reg} cell-mediated immune homeostasis.

However, deletion of FASN in T_{reg} cells inhibited the growth of MC38 and B16 tumors (Fig. 3c, d). Similar as the observations of SCAP deletion, these effects were restricted to the TME, as EAE disease score (Extended Data Fig. 7j) and CNS inflammation (Extended Data Fig. 7k) were comparable between control and $Foxp3^{Cre}Fasn^{fl/fl}$ mice. Similarly, the proportion of CD8$^+$ T cells producing TNF-α, although not IFN-γ, was increased in $Foxp3^{Cre}Fasn^{fl/fl}$ mice in tumours specifically (Extended Data Fig. 8a), which was not observed in Foxp3$^-$CD4$^+$ T cells (Extended Data Fig. 8b). However, unlike $Foxp3^{Cre}Scap^{fl/fl}$ mice, tumours isolated from $Foxp3^{Cre}Fasn^{fl/fl}$ mice showed largely normal cellularity and activation state of CD8$^+$ and Foxp3$^-$CD4$^+$ T cells (Extended Data Fig. 8c–f). Also, FASN deletion did not alter the accumulation of intratumoural T_{reg} cells, the ratio of CD8$^+$ T cells versus T_{reg} cells, or T_{reg} cell IFN-γ production (Extended Data Fig. 8g–i).

To profile the functional state of FASN-deficient T_{reg} cells in tumours, we performed transcriptome analysis of intratumoural T_{reg} cells and found that fatty acid metabolism pathway was downregulated in FASN-deficient T_{reg} cells (Extended Data Fig. 8j). Of note, T_{reg} cell-specific TCR-dependent gene signature[29] was also downregulated (Extended Data Fig. 8k). We hypothesized that FASN signalling contributes to TCR-dependent T_{reg} cell activation and/or functional maturation[29,30]. Indeed, while freshly-isolated FASN-deficient T_{reg} cells had normal suppressive function *in vitro* (Extended Data Fig. 8l), following TCR stimulation[21], FASN-deficient T_{reg} cells had reduced function (Fig. 3e). To link FASN with fatty acid synthesis, we added exogenous palmitate, an enzymatic product of FASN, to FASN-deficient T_{reg} cells and found that palmitate restored their suppressive function (Fig. 3e). Additionally, despite normal TCR-induced proliferation (Extended Data Fig. 8m),

FASN deletion impaired TCR-dependent upregulation of T_{reg} cell activation/maturation markers including GITR and CD44[30] (Extended Data Fig. 8n). GITR and CD44 were also reduced on FASN-deficient T_{reg} cells in tumours, not PLNs (Extended Data Fig. 8o). These data collectively indicate that FASN signalling contributes to TCR-induced functional maturation of T_{reg} cells.

We next explored additional mechanisms that may act downstream of SCAP/SREBP activation. Our scRNA-seq analysis revealed that intratumoural SCAP-deficient T_{reg} cells had reduced expression of *Pdcd1* (encoding PD-1) (Extended Data Fig. 9a). Flow cytometry analysis also showed that PD-1 expression was substantially reduced on SCAP-deficient T_{reg} cells in tumours, not in PLNs (Fig. 3f). In contrast, SCAP-deficient T_{reg} cells had normal expression of the T_{reg} cell signature molecules, CTLA4, ICOS, CD69, CD25, Nrp-1, CD39 and CD73 (Fig. 3f and Extended Data Fig. 9b). Additionally, PD-1 expression on T_{reg} cells was unaltered in the spleen or non-lymphoid organs from *Foxp3*[Cre]*Scap*^{fl/fl} mice under steady state (Extended Data Fig. 9c). Thus, SCAP/SREBP signalling is required for PD-1 expression on T_{reg} cells in tumours, but not in the peripheral lymphoid and non-lymphoid tissues. PD-1 has been shown to dampen PI3K signalling[31], and PI3K activation is associated with elevated IFN-γ production by T_{reg} cells[24,25]. Consistent with a previous report[25], anti-PD-1 treatment increased IFN-γ expression in T_{reg} cells (Extended Data Fig. 9d). Importantly, following anti-PD-1 treatment, T_{reg} cells upregulated p-AKT and p-S6 levels in tumours, but not PLNs (Fig. 3g, h). Moreover, T_{reg} cells deficient in SCAP also showed increased p-AKT and p-S6 levels in tumours, further supporting a role for SCAP and PD-1 signalling in shaping PI3K activity in intratumoural T_{reg} cells (Fig. 3i, j). Collectively, these results suggest that SCAP/SREBP and PD-1 repress IFN-γ expression and PI3K signalling in intratumoural T_{reg} cells.

To determine the effects of the TME and other contexts on PD-1 expression on T_{reg} cells, we examined PD-1 regulation in different models. PD-1 expression was induced on intratumoural T_{reg} cells as compared to those in the spleen (Fig. 4a). Additionally, *Pdcd1* mRNA expression was upregulated in tumour-infiltrating T_{reg} cells as compared to peripheral T_{reg} cells in public scRNA-seq datasets of mouse melanoma models[7,8] (Extended Data Fig. 9e, f) and human patients with HNSCC[10] (Fig. 4b) or breast cancer[9] (Extended Data Fig. 9g). However, induction of PD-1 expression on T_{reg} cells was not observed in the EAE model (Fig. 4a), suggesting context-selective regulation. In contrast, expression of CTLA4 and ICOS was upregulated in T_{reg} cells from both tumours and EAE (Extended Data Fig. 9h, i). Next, we determined how PD-1 expression is regulated at the molecular level by SREBP signalling. Consistent with the aforementioned surface protein regulation (Fig. 3f), *Pdcd1* but not *Icos* mRNA expression in SCAP-deficient T_{reg} cells was reduced in tumours, while no difference was observed in PLNs (Fig. 4c), indicating a role of SREBP signalling in *Pdcd1* expression in intratumoural T_{reg} cells.

To determine the upstream signals that regulate PD-1 expression, we performed transcriptome analysis of PD-1^{hi} and PD-1^{lo} T_{reg} cells isolated from the TME. T_{reg} cell-specific TCR-dependent gene signature[29] was modestly enriched in PD-1^{hi} cells (Extended Data Fig. 9j). Addition, PD-1^{hi} T_{reg} cells had higher expression of Nur77-GFP, a specific reporter for TCR signalling[32] (Fig. 4d). Moreover, PD-1 expression was upregulated on T_{reg}

cells in response to *in vitro* TCR stimulation (Extended Data Fig. 9k), indicating TCR-dependent induction of PD-1 expression. TCR stimulation also upregulated expression of SREBP gene targets (Extended Data Fig. 9l, m). Importantly, deletion of SCAP in T_{reg} cells impaired TCR-induced expression of surface PD-1 (Fig. 4e) and *Pdcd1* mRNA *in vitro* (Extended Data Fig. 9n). Thus, SCAP/SREBP signalling links TCR stimulation to PD-1 expression on T_{reg} cells.

SREBPs regulate the expression of enzymes for both fatty acid synthesis and mevalonate metabolism[6]. Of note, fatty acid synthesis is dispensable for PD-1 expression, as PD-1 levels were unperturbed on intratumoural FASN-deficient T_{reg} cells (Extended Data Fig. 10a). We therefore tested the involvement of mevalonate metabolism, which contributes to synthesis of cholesterol and isoprenoids[6,33]. SCAP-deficient T_{reg} cells had reduced incorporation of [$^{13}C_2$]acetate-derived carbons into cholesterol as determined by metabolomic tracing analysis (Fig. 4f). Treatment with simvastatin that targets HMGCR, a rate-limiting enzyme in mevalonate metabolism, inhibited PD-1 expression on TCR-stimulated T_{reg} cells (Fig. 4g). Additionally, HMGCR-deficient T_{reg} cells had defective PD-1 expression on TCR stimulation (Extended Data Fig. 10b). However, cholesterol supplementation to SCAP-deficient T_{reg} cells, which partially rectified the proliferative defect (Extended Data Fig. 5d) as well as upregulation of CTLA4 (Extended Data Fig. 10c), did not affect PD-1 expression (Extended Data Fig. 10d). These results reveal the importance of cholesterol-independent mevalonate metabolism for PD-1 regulation in T_{reg} cells.

In addition to cholesterol, the mevalonate pathway generates the isoprenoids farnesylpyrophosphate (FPP) and geranygeranylpyrophosphate (GGPP)[33], lipid molecules that mediate protein post-translational modifications of farnesylation and geranylgeranylation via the enzymatic activities of farnesyltransferase (catalytic subunit encoded by *Fntb*) and geranylgeranyltransferase type I (catalytic subunit encoded by *Pggt1b*), respectively. Therefore, we tested the effects of FPP and GGPP on PD-1 regulation. As expected, mevalonate, the metabolite directly downstream of HMGCR, rescued PD-1 expression on simvastatin-treated T_{reg} cells (Fig. 4h). Importantly, GGPP treatment also restored PD-1 expression on cells, while FPP showed only a minor rescue effect (Fig. 4h). Additionally, mevalonate or GGPP treatment also largely rescued *Pdcd1* mRNA expression in simvastatin-treated T_{reg} cells (Extended Data Fig. 10e). These results suggest a possible role of GGPP-dependent protein geranylgeranylation in promoting PD-1 expression on T_{reg} cells. In support of this notion, treatment with the geranylgeranyltransferase type I inhibitor GGTI (GGTI-2147)[33] strongly inhibited TCR-induced PD-1 expression on T_{reg} cells, while the farnesyltransferase inhibitor FTI (FTI-277)[33] showed a small effect (Extended Data Fig. 10f). Moreover, T_{reg} cells deficient in *Pggt1b* (Extended Data Fig. 10g), but not *Fntb* (Extended Data Fig. 10h), had reduced TCR-induced PD-1 expression *in vitro*, thereby validating the results from the pharmacological inhibitors. Protein geranylgeranylation promotes Rac signalling and activity of AP-1 transcription factors in T_{reg} cells[34], the latter of which is implicated in PD-1 regulation[35]. Indeed, PD-1 induction upon TCR stimulation was impaired on T_{reg} cells deficient in Rac1 and Rac2 (Extended Data Fig. 10i), or upon treatment with AP-1 inhibitors (Extended Data Fig. 10j). Collectively, these data reveal metabolic dependence of PD-1 expression on T_{reg} cells through a signalling axis composed

of SCAP/SREBP, mevalonate metabolism, protein geranylgeranylation and downstream Rac signalling.

T_{reg} cells accumulate into tumours and hinder effective antitumour immune responses, and represent a promising target for cancer immunotherapy[2]. However, given the overall importance of T_{reg} cells in maintaining immune homeostasis and tissue integrity[1], therapeutic targeting of T_{reg} cells shows limited efficacy or leads to autoimmunity. Emerging studies uncover context-specific functional reprogramming of T_{reg} cells in tissues, including the identification of surface receptors involved in this process[22,25]. Recent studies also reveal that intratumoural T_{reg} cells actively maintain functional integrity to prevent fragility in the TME[25,26]. However, whether and how T_{reg} cell functional fitness can be shaped by intracellular metabolic networks in the TME remain largely unknown. By combining unbiased systems approaches and comprehensive genetic tools, we demonstrate that intratumoural T_{reg} cells actively rewire SREBP-dependent *de novo* lipid biosynthesis, which acts to maintain T_{reg} cell state and function in the TME. Mechanistically, SREBPs coordinate FASN-dependent fatty acid synthesis and mevalonate metabolism-dependent induction of *Pdcd1* expression (Extended Data Fig. 10k).

While co-inhibitory receptors, including PD-1, have been implicated in T_{reg} cell functional fitness[13,31,36], the regulation of their expression and functional importance in intratumoural T_{reg} cells remain poorly understood. Here we reveal tumour-selective induction of PD-1 expression on T_{reg} cells and define metabolic dependence of PD-1 expression on intratumoural T_{reg} cells through a novel metabolic signalling axis comprised of SCAP/ SREBP, mevalonate metabolism, and protein geranylgeranylation, which further links to Rac signalling. We further show that SCAP/SREBP signalling and PD-1 function in intratumour T_{reg} cells are important for proper control of PI3K signalling and IFN-γ production, which are detrimental to T_{reg} cell suppressive function[24], including in the TME[25,26]. Our results also indicate that PD-1 and FASN play discrete effects in T_{reg} cell functional fitness, with FASN contributing to TCR-induced T_{reg} cell functional maturation but not IFN-γ production. From a therapeutic point of view, future studies are warranted to determine the extent to which T_{reg} cells in the TME are sensitive to inhibition of SREBP and lipid metabolism relative to other cells[37,38]. Collectively, our results establish metabolic rewiring of intratumoural T_{reg} cells to enforce functional specialization in the TME and reveal new cellular and molecular targets for cancer immunotherapy.

METHODS

Mice

Rag1^{−/−}, *Scap*^{fl/fl}, *Fasn*^{fl/fl}, *Rac1*^{fl/fl}, *Rac2*^{−/−}, Nur77-GFP, *Foxp3*[DTR], *Foxp3*[RFP], *Rosa26*[YFP] reporter (a *lox*P-site-flanked STOP cassette followed by the YFP-encoding sequence was inserted into the *Rosa26* locus), and C57BL/6 mice were purchased from the Jackson Laboratory. *Foxp3*[YFP-Cre] and *Foxp3*[GFP-Cre-ERT2] mice were from A. Rudensky[14,39]. *Fntb*^{fl/fl} and *Pggt1b*^{fl/fl} mice were from M. Bergo[40,41]. *Hmgcr*^{fl/fl} mice were as described previously[42]. All genetic models were on the C57BL/6 background. Both male and female mice were used for analysis and quantification. *Foxp3*[Cre]*Scap*^{fl/fl}, *Foxp3*[Cre]*Fasn*^{fl/fl} and *Foxp3*[Cre]*Hmgcr*^{+/fl} mice were used at 7–18 weeks old, unless otherwise noted, with age- and

sex-matched $Foxp3^{Cre}$-containing mice as controls. $Foxp3^{Cre}Hmgcr^{fl/fl}$, $Foxp3^{Cre}Fntb^{fl/fl}$, $Foxp3^{Cre}Pggt1b^{fl/fl}$ and $Rac1^{fl/fl}Rac2^{-/-}$ mice were used at less than 3 weeks old due to systemic inflammation, with age- and sex-matched $Foxp3^{Cre}$-containing mice as controls. In selective experiments, bone marrow chimeras were generated by transferring 5×10^6 T cell-depleted bone marrow cells into sublethally irradiated (5 Gy) $Rag1^{-/-}$ mice, to expand the cohort of mice for the desired genotypes. $Foxp3^{Cre/DTR}$ mosaic mice were treated with DT (50 μg/kg) *i.p.* three times per week, for a total of four injections. The mice were euthanized, and tissues were harvested for flow cytometry analysis eleven days following the first DT treatment[16,17]. All mice were kept in a specific pathogen-free facility in the Animal Resource Center at St. Jude Children's Research Hospital. Animal protocols were approved by the Institutional Animal Care and Use Committee of St. Jude Children's Research Hospital.

Flow cytometry

For surface marker analysis, cells were stained in PBS containing 2% (w/v) BSA and the appropriate antibodies. Surface proteins were stained for 20 min on ice. Intracellular staining was performed with the Foxp3/transcription factor staining buffer set, according to the manufacturer's instructions (eBioscience). For intracellular cytokine staining, cells were stimulated for 4 h with PMA plus ionomycin in the presence of monensin before being stained according to the manufacturer's instructions using the Cytofix/Cytoperm™ fixation/permeabilization kit (BD Biosciences). Active caspase-3 staining was performed using instructions and reagents from the Active Caspase-3 Apoptosis Kit (BD Biosciences). BrdU staining (pulsed for 18 h) was performed using instructions and reagents from the APC BrdU Flow Kit (BD Biosciences). 7AAD (Sigma) or fixable viability dye (eBioscience) was used for dead-cell exclusion. The following fluorescent conjugate-labelled antibodies were used: anti-CD4 (RM4–5), anti-CD8α (53–6.7), anti-TCRβ (H57–597) (all from Tonbo Biosciences); anti-CD25 (PC61.5), anti-CD44 (1M7), anti-CD62L (MEL-14), anti-CD45.2 (104), anti-ICOS (C398.4A), anti-PD-1 (J43), anti-CD36 (CRF D-2712) (all from BD Biosciences); anti-Foxp3 (FJK-16s), anti-IFN-γ (XMG1.2), anti-IL-4 (11B11), anti-IL-17 (17B7), anti-GITR (DTA-1), anti-TIM3 (RMT3–23) (all from eBioscience); anti-CD69 (H1.2F3), anti-CD39 (Duha59), anti-CD73 (TY/11.8), anti-Nrp-1 (3E12), anti-TNF-α (MP6-XT22) and anti-CTLA4 (UC10–4B9) (all from BioLegend). To monitor cell division, lymphocytes were labelled with CellTrace™ Violet (Life Technologies). For detection of phosphorylated signalling proteins, lymphocytes were rested in a complete medium for 1 h, and then fixed with Phosflow Lyse/Fix buffer, followed by permeabilization with Phosflow Perm buffer III (BD Biosciences) and staining with antibodies to S6 phosphorylated at Ser 235 and Ser 236 (D57.2.2E) and AKT phosphorylated at Thr 308 (D25E6) (all from Cell Signaling Technology). To measure fatty acid uptake, intratumoural T_{reg} cells were resuspended in HBSS containing 5 mg/ml BODIPY FL C12 (Life Technologies) at a final concentration of 0.5 μM and incubated in the dark for 30 min at 37 °C. Cells were then washed twice with PBS to remove staining solution, followed by standard surface staining. For mitochondrial staining, lymphocytes were incubated for 30 min at 37 °C with 10 nM MitoTracker Deep Red (Life Technologies), 20 nM TMRM (ImmunoChemistry Technologies) or 5 μM MitoSOX Red (Life Technologies) after staining surface markers[43]. Flow cytometry data were acquired on a LSRII or LSR Fortessa (BD Biosciences) and

analyzed using Flowjo software (Tree Star). $TCR\beta^+$ was used to define $CD4^+$ and $CD8^+$ T cells throughout this study.

Tumour model and tumour-infiltrating lymphocyte isolation

MC38 colon adenocarcinoma cells were maintained in the laboratory and cultured in RPMI 1640 medium supplemented with 10% (vol/vol) fetal bovine serum (FBS) and 1% (vol/vol) penicillin-streptomycin. B16-F10 melanoma cells were maintained in the laboratory and cultured in DMEM (Dulbecco's modified essential medium) supplemented with 10% (vol/vol) FBS and 1% (vol/vol) penicillin-streptomycin. Mice were injected subcutaneously with 5×10^5 MC38 colon adenocarcinoma cells or 2×10^5 B16-F10 melanoma cells in the right flank[43]. Tumours were measured regularly with digital calipers and tumour volumes were calculated by the formula: Length $\times$ Width $\times$ [(Length $\times$ Width)$^{0.5}$] $\times \pi/6$. Tamoxifen was injected *i.p.* daily as indicated. Anti-PD-1 (200 μg; clone 29F.1A12) or rat IgG2a isotype control antibodies (200 μg; clone 2A3) were injected *i.p.* four times in 100 μl PBS on days 7, 10, 13 and 16 after tumour cell injection. Anti-CD8α antibodies (200 μg; clone YTS169.4) were injected in 100 μl PBS on days –1, 2, 5, 8, 11. To prepare tumour-infiltrating lymphocytes (TILs)[43], tumour was excised, minced and digested with 1 mg/ml Collagenase IV (Roche) + 200 U/ml DNase I (Sigma) for 1 h at 37 °C. TILs were isolated by density-gradient centrifugation over Percoll (Life Technologies).

EAE induction

Mice were immunized subcutaneously at four injection sites with a total of 200 μl of emulsified incomplete Freund's adjuvant supplemented with 1 mg *Mycobacterium tuberculosis* strain H37Ra (Difco) (complete Freund's adjuvant; CFA) and 200 μg myelin oligodendrocyte glycoprotein (amino acids 35–55; MOG_{35-55}), and received *i.p.* injections of 200 ng pertussis toxin (PTX; List Biological Laboratories) at the time of immunization and 48 h later[44]. Mice were observed daily for clinical signs and scored as follows: 0, no overt signs of disease; 1, limp tail; 2, limp tail plus hindlimb weakness; 3, total hindlimb paralysis; 4, hindlimb paralysis plus 75% of body paralysis (forelimb paralysis/weakness); 5, moribund.

Cell purification and culture

Unless otherwise noted, lymphocytes were isolated from spleen and PLNs (including axillary, inguinal and cervical lymph nodes; the same number of PLNs were collected from each mouse) and T_{reg} cells ($CD4^+Foxp3-YFP^+$) were sorted on a MoFlow (Beckman-Coulter) or Reflection (i-Cyt). Sorted cells were cultured in plates coated with anti-CD3 (2C11, 10 μg/ml) and anti-CD28 (37.51, 10 μg/ml; both from Bio X cell) for the indicated times in Click's medium (Irvine Scientific) supplemented with β-mercaptoethanol, 10% (v/v) FBS, 1% (v/v) penicillin-streptomycin and IL-2 (200 U/ml). In selective experiments, GGTI-2147 (5 μM) (Calbiochem), FTI-277 (10 μM) (Tocris), cholesterol (4.5 μg/ml) (Sigma), simvastatin (2 μM) (Cayman Chemicals), Sr11302 (Tocris), T-5224 (Cayman Chemicals) and BSA-palmitate saturated fatty acid complex (100 μM) (Cayman Chemicals) were added to the culture. T_{reg} cells were pre-treated with inhibitors for 1 h and then stimulated with 10 μg/ml anti-CD3/28 antibodies plus 200 U/ml IL-2 in the presence of inhibitors. Mevalonate (500 μM) (Sigma), FPP (50 μM) (Sigma), and GGPP (5 μM) (Sigma)

were added to the culture. Cells were harvested for flow cytometry analysis at different time points as indicated in figure legends. *In vitro* T_{reg} cell suppression assays were performed as described[45]. Briefly, freshly-sorted naïve $CD4^+$ T cells (T_N; $CD4^+CD62L^+CD44^{lo}CD25^-$; 5×10^4) and T_{reg} cells (at different ratios with T_N cells) were cultured in 96-well plates along with anti-CD3 antibody and irradiated splenocytes for 72 h, followed by thymidine incorporation assays. For T_{reg} cell suppression assays using previously activated T_{reg} cells, T_{reg} cells were activated with anti-CD3/CD28 antibodies plus IL-2 for 3 days in the absence or presence of BSA-palmitate-saturated fatty acid complex. Viable T_{reg} cells were purified using Ficoll and incubated with freshly-isolated T_N cells for additional analysis as described earlier.

Histology

Tissue were fixed by 10% (vol/vol) neutral buffered formalin solution, embedded in paraffin, sectioned and stained with hematoxylin and eosin, and the clinical signs of autoimmune diseases and EAE were analyzed by an experienced pathologist (P. Vogel)[44].

T_{reg} cell *in vivo* transfer and expansion

For adoptive transfer, T_{reg} cells from *Foxp3*[Cre]*Scap*^{+/fl} mice and *Foxp3*[Cre]*Scap*^{fl/fl} mice were transferred to *Rag1*^{−/−} mice[24]. Fourteen days after the transfer, recipients were euthanized for the analysis of transferred cells. To prepare IL-2/anti-IL-2 complex[19,20], 2 μg recombinant mouse IL-2 (Peprotech) and 10 μg anti-IL-2 (JES6–1) were mixed in 200 μl PBS and incubated at 37 °C for 30 min. Mice received *i.p.* injection of IL-2/anti-IL-2 complex on days 0, 1 and 2, and were analyzed on day 5.

RNA isolation and real-time PCR

RNA was isolated using the RNeasy Micro Kit (Qiagen 74004) following the manufacturer's instructions. RNA was converted to cDNA using the High Capacity cDNA Reverse Transcription Kit (Thermo Fisher Scientific 4368813) according to manufacturer's instructions. Real-time PCR was performed on the QuantStudio 7 Flex System (Applied Biosystems) using the following probes: *Actb* (Mm 00697939), *Pdcd1* (Mm 00435532), *Ctla4* (Mm 00486849), *Icos* (Mm 00497600) and *Fasn* (Mm01253304) (all from Thermo Fisher Scientific). The primers for SYBR Green master mix were *Hmgcr* (forward: 5'-AGCTTGCCCGAATTGTATGTG-3', reverse: 5'-TCTGTTGTGAACCATGTGACTTC-3'), *Scap* (forward: 5'- TCCAAACACCGGACCGC-3', reverse: 5'-AGGGTCATCCTCGGCTAAGT

−3'), and *Actb* (forward: 5'-GACAGGATGCAGAAGGAGATTACTG-3', reverse: 5'-GCTGATCCACATCTGCTGGAA-3').

Serum autoantibody measurement

Anti-dsDNA antibodies and anti-nuclear antigens (ANA) antibodies were measured with kits from Alpha Diagnostic International (5110 and 5210, respectively).

Gene expression profiling, gene set enrichment analysis (GSEA) and Ingenuity pathway analysis (IPA)

Microarray analyses (Affymetrix Mouse Clariom S Assay) of total RNA collected in individual batches from the following T_{reg} cell samples were performed: (a) T_{reg} cells from tumours or PLNs of *Foxp3*[Cre]*Scap*[+/+ or +/fl] ($n = 4$ biological replicates) or *Foxp3*[Cre]*Scap*^{fl/fl} ($n = 3$ biological replicates) mice bearing B16 melanoma; (b) T_{reg} cells from tumours of *Foxp3*[Cre]*Fasn*[+/+ or +/fl] or *Foxp3*[Cre]*Fasn*^{fl/fl} mice bearing B16 melanoma ($n = 3–4$ biological replicates each group); (c) PD-1^{hi} or PD-1^{lo} (top and bottom 10%) T_{reg} cells from tumours of *Foxp3*[RFP] mice bearing MC38 colon adenocarcinoma ($n = 4$ biological replicates each group); and (d) T_{reg} cells (from *Foxp3*[Cre] mice) stimulated with anti-CD3/28 antibodies for 0 h and 8 h ($n = 5$ biological replicates per time point). For microarray analyses[43], the expression signals were summarized using the robust multi-array average algorithm (Affymetrix Expression Console v1.1), followed by differential expression (DE) analysis performed using R package limma v.3.34.9. All the plots were generated using R package ggplot2 v.2.2.1. The Benjamini-Hochberg method was used to estimate the false discovery rate (FDR) as described[21]. DE genes were defined by $|\log_2$ fold change (FC)$| > 0.5$; $P < 0.05$. GSEA was performed as described[46] using the "Hallmark" database or cell metabolism-related pathways curated from the KEGG and Reactome databases (Supplementary Table 1). For GSEA using manually curated gene signatures from public datasets, a public microarray dataset (GSE61077)[29] was used for generating the "T_{reg} cell-specific TCR gene signature" (genes downregulated in TCRα-deficient aT_{reg} cells compared to TCRα-sufficient aT_{reg} cells) (< 5% FDR). The "direct SREBP targets" was derived from a public dataset[47] [genes upregulated in SREBP-1a- or SREBP-2-transgenic mice but downregulated in the absence of SCAP (SREBP cleavage-activating protein)]. DE genes generated by comparing Foxp3-YFP[+] T_{reg} cells from tumours versus PLNs of *Foxp3*[Cre]*Scap*[+/+ or +/fl] mice were used for IPA of upstream transcriptional regulators[24]. The top 15 upstream transcriptional regulators were plotted with their activation z-score and P value indicated.

Single-cell RNA sequencing (scRNA-seq) and data analysis

Library preparation—*Foxp3*[Cre]*Scap*[+/+ or +/fl] and *Foxp3*[Cre]*Scap*^{fl/fl} mice were challenged with B16 melanoma, and CD45.2[+] TILs were sorted on a Reflection cell sorter (iCyt) ($n = 2$ biological replicates each group). Foxp3-YFP[+] T_{reg} cells were isolated from the spleen and CNS (spinal cord and brain) of *Foxp3*[Cre] mice at the peak of EAE (day 15) after MOG immunization ($n = 1$ each group). The cells were counted and examined for viability using a Luna Dual Florescence Cell Counter (Logos Biosystems). All samples were spun down at 2,000 rpm for 5 min. The supernatant was removed, and cells were resuspended in 100 μl of 1× PBS (Thermo Fisher Scientific) + 0.04% BSA (Amresco). The cells were then counted and examined for viability using a Luna Dual Florescence Cell Counter (Logos Biosystems). Cell counts were approximately $1×10^6$ cells/ml and viability was above 98%. Single-cell suspensions were loaded onto the Chromium Controller according to their respective cell counts to generate 8,000 single-cell gel beads in emulsion per sample. Each sample was loaded into a separate channel. Libraries were prepared using the Chromium Next GEM Single Cell 3′ v.3.1 Library and Gel Bead Kit (10X Genomics). The cDNA content of each

sample after cDNA amplification of 12 cycles was quantified and quality-checked using a High-Sensitivity DNA chip with a 2100 Bioanalyzer (Agilent Technologies) to determine the number of PCR amplification cycles to yield a sufficient library for sequencing. After library quantification and quality-checking using DNA 1000 chip (Agilent Technologies), samples were diluted to 3.5 nM for loading onto the HiSeq 4000 (Illumina) with a 2×75-bp paired-end kit using the following read length: 26-bp read 1, 8-bp i7 index, and 98-bp read 2. An average of 4×10^8 reads per sample were obtained (approximately 8×10^4 reads per cell).

Alignment, barcode assignment and unique molecular identifier (UMI) counting—The Cell Ranger 1.3 Single-Cell software suite (10X Genomics) was implemented to process the raw sequencing data from the Illumina HiSeq run[43]. This pipeline performed demultiplexing, alignment (using the mouse genome mm10 from ENSEMBL GRCm38) and barcode processing to generate gene–cell matrices. Seurat R package (v3.1.2)[48] was used for downstream analysis. Specifically, data from CD45$^+$ TIL samples, isolated from $Foxp3^{Cre}Scap^{+/+ \text{ or } +/fl}$ and $Foxp3^{Cre}Scap^{fl/fl}$ mice ($n = 2$ per genotype), were combined into one dataset for consistent filtering. Cells with low unique molecular identifier (UMI) counts (potentially dead cells with broken membranes) or high UMI counts (potentially two or more cells in a single droplet) were filtered. Cells with high percent ($> 8.37\%$) of mitochondrial reads were also removed. Residual CD45$^-$ contaminants introduced by cell sorting were further removed, together with B cells. A total of 30,679 cells ($Foxp3^{Cre}Scap^{+/+ \text{ or } +/fl}$ mice, 14,558; $Foxp3^{Cre}Scap^{fl/fl}$ mice, 16,121) were captured, with an average of 2,411 mRNA molecules (UMIs, median: 6,488; range: 500–246,680). For T$_{reg}$ cell data from the EAE mouse model, cells with a high percentage ($> 8\%$) of mitochondrial reads were removed. A total of 6,669 cells (CNS, 2,736; spleen, 3,933) were captured, with an average of 1,643 mRNA molecules (UMIs, median: 4,042; range: 2,022–29,517). We normalized the expression level of each gene to 100,000 UMIs per cell and log-transformed them by adding 1 to the expression matrix.

Data visualization—To identify different clusters in TILs, data were further analyzed using Seurat and visualized by UMAP [Uniform Manifold Approximation and Projection[49]], which partitioned cells into 22 unsupervised clusters based on their transcriptomes using resolution = 0.5 in FindClusters function. Fourteen immune cell types were further identified based on prior knowledge and markers highly expressed in each unsupervised cluster. For data from EAE mouse model, T$_{reg}$ cells from the CNS and spleen were visualized by UMAP. The activity of SREBP signalling was calculated by the average expression of all of the target genes in the gene set and color-coded (from low to high, blue–red) on the UMAP visualization. Curated violin plots that represent the expression level of genes were generated by VlnPlot function in Seurat R package.

Metabolomic tracing studies

Cell sample collection—T$_{reg}$ cells were stimulated with anti-CD3/28 antibodies plus IL-2 in the presence of 2 mM [$^{13}C_2$]-sodium acetate for 2 days. Cells were then collected by a brief centrifugation, washed once with ice-cold saline, centrifuged again and then the tubes

with the cell pellets were flash-frozen in liquid nitrogen. The cell pellets were stored at −80 °C until the extraction of metabolites.

Extraction of hydrophilic metabolites and lipids—To extract hydrophilic molecules, an adapted three-phase solvent system was utilized to separate hydrophilic metabolites from lipids, protein and nucleic acids[50]. Briefly, the cell pellets were resuspended in 0.2 ml of ice-cold saline and then 1 ml of chloroform/methanol (2:1, v/v) was added. Next, the mixture was homogenized using a Bead Ruptor Elite (OMNI international, Kennesaw GA, USA) for 30 sec at 8 m/s, and the homogenate was centrifuged for 15 min at 21,000 g at 4 °C. After centrifugation, the upper aqueous phases were transferred into new tubes, froze on dry-ice and then dried by lyophilization. The lower organic phases were transferred into new tubes and then dried under a stream of nitrogen at room temperature.

LC-MS analysis of isotopic labelling—A Vanquish Horizon UHPLC (Thermo Scientific) was used for the LC separations, using a linear gradient condition (0–1 min 50% B; 1–5.5 min 50 to 99% B; 5.5–8 min 99% B; 8–8.5 min 99 to 50% B; 8.5–10 min 50% B), mobile phase A [water/acetonitrile (6:4, v/v)], and mobile phase B [isopropanol/acetonitrile (9:1, v/v)]; both A and B contained 10 mM ammonium acetate. The column used was a Thermo Scientific Accucore C30 (2.1×50 mm, 2.6 μm) operated at 40 °C. The flow rate was 250 μl/min and the injection volume was 10 μl. All LC/MS solvents and reagents were the highest purity available (water, acetonitrile, isopropanol, ammonium acetate) purchased from Thermo Fisher Scientific. An authentic cholesterol standard was purchased from Sigma-Aldrich. A Thermo Scientific Q Exactive hybrid quadrupole-Orbitrap mass spectrometer (QE-MS) equipped with an APCI probe was employed as detector. The QE-MS was operated in the positive mode, using a targeted selected ion monitoring method (t-SIM/dd-MS^2). The mass spectrometer was operated at a resolution of 140,000 (FWHM, at m/z 200); AGC targeted 2×10^5; max injection time 100 msec; loop count 2; and isolation width 0.5 m/z. For the dd-MS^2 conditions, a resolution of 17,500 was used with AGC targeted 1×10^5, max injection time 50 msec, loop count 2, MS^2 isolation width 0.5 m/z, NCE 35. The APCI source operating conditions were: sheath gas flow 15, auxiliary gas flow 20, sweep gas 1, discharge current 10 μA, capillary temperature 325 ℃, S-lenses RF level 65, vaporizer temperature 325 °C. The ions targeted for cholesterol analysis (parent/daughters m/z) were 369.3514/215.1792/175.1481. The data were tabulated as the peak area from each LC/MS chromatography, extracted from the tSIM parent mass (at 5 ppm mass tolerance). For all the LC-MS analyses indicate above [with the exception of the targeted selected ion monitoring methods (t-SIM/dd-MS^2)], wide-range of MS^1 spectra scans (Full-MS) were also acquired during the entire duration of each chromatography. The Full-MS data were acquired at a resolution of 140,000 (FWHM, at m/z 200), using an AGC target of 1×10^6, a max injection time of 80 msec and a scan range from 100 to 1,000 m/z. From the actual m/z values of every targeted molecule, exact masses were calculated for every potential labelling proceeding from [$^{13}C_2$]-sodium acetate, and then every potentially labelled m/z was searched in the Full-MS data, at the retention times of their corresponding unlabeled molecules. The data from each potentially labelled-molecule were tabulated as the peak areas extracted from the Full-MS parent masses (at 100 ppm mass tolerance). True labelling was assessed in the [$^{13}C_2$]-sodium acetate treated samples after carefully

determining that the peak areas of every potential labelled-m/z was significantly increased when compared to the cold-acetate treated samples. The total contribution of carbon was calculated using the following equation after subtracting naturally occurring isotopes[51]:

$\sum_{i=0}^{n} i \times m_i / \left(n \sum_{i=0}^{n} m_i \right)$ where n is the number of C atoms in the metabolite, i represents the different mass-isotopomers, and m refers to the abundance of a certain mass.

Statistical analysis for biological experiments

For experimental data, we tested the normal distribution, and Prism 6 software (GraphPad) was used to analyze biological experiment (non-omics) data by performing two-tailed unpaired Student's t-test. When multiple groups were compared, one-way ANOVA with the Tukey's test was performed. Two-way ANOVA was performed for comparing tumour growth curves and EAE disease development curves. P value of less than 0.05 was considered significant. Data are presented as mean ± s.e.m.

Extended Data
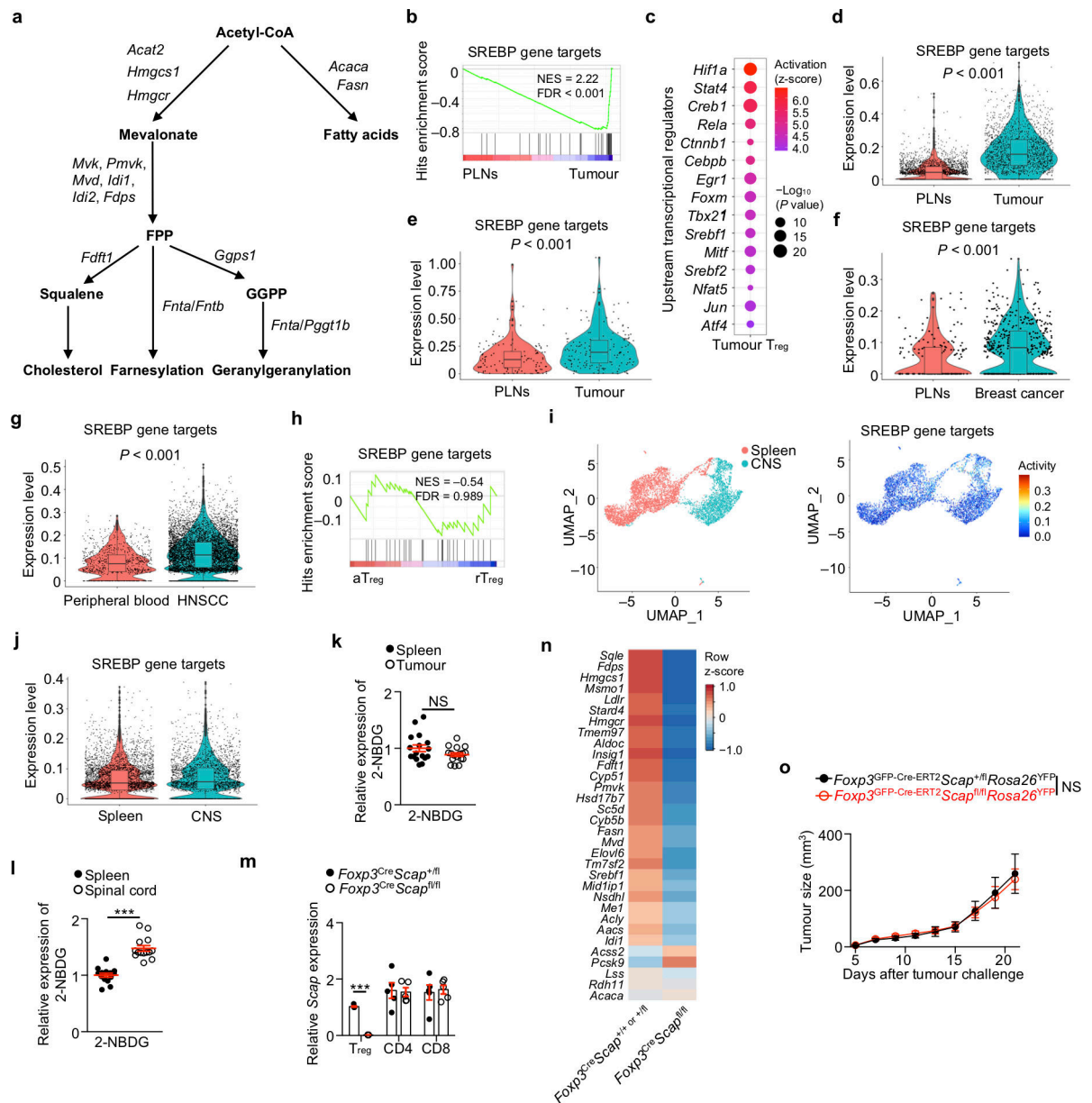
Extended Data Figure 1. Different metabolic states of T_{reg} cells in tumours and inflammatory contexts.

(**a**) Diagram of *de novo* lipid synthesis biochemical pathways. (**b**) Enrichment plots of SREBP gene targets in intratumoural versus PLN-derived T_{reg} cells from B16 melanoma-bearing *Foxp3*[Cre] mice. (**c**) Top 15 upstream transcriptional regulators enriched in intratumoural T_{reg} cells as compared to PLN T_{reg} cells from B16 melanoma-bearing *Foxp3*[Cre] mice, analyzed by Ingenuity pathway analysis. (**d, e**) Enrichment of SREBP gene targets in intratumoural and PLN T_{reg} cells from public mouse B16 melanoma scRNA-seq datasets[7,8]. (**f, g**) Enrichment of SREBP gene targets in intratumoural T_{reg} cells from human patients with breast cancer[9] (**f**) and HNSCC[10] (**g**). (**h**) Enrichment plots of SREBP gene

targets from the public dataset[11] of *in vivo* activated T_{reg} (aT_{reg}) compared to resting T_{reg} (rT_{reg}) cells in the acute inflammation model. (**i, j**) T_{reg} cells were isolated from spleen and CNS of MOG-induced *Foxp3*[RFP] EAE mice for scRNA-seq analysis. (**i**) Unsupervised clustering of cells in the spleen and CNS was analyzed by UMAP, with the splenic and CNS cells annotated with different colors (left), and the expression of SREBP gene targets visualized on the UMAP plot (right). (**j**) Comparison of SREBP gene targets between splenic and CNS T_{reg} cells on the UMAP plot. (**k**) Relative (values in splenic samples were set to 1) uptake of a fluorescent glucose analog, 2-(N-(7-nitrobenz-2-oxa-1,3-diazol-4-yl)amino)-2-deoxyglucose (2-NBDG), in splenic and intratumoural T_{reg} cells from MC38 tumour-bearing mice on day 21 after tumour inoculation ($n = 17$). (**l**) Relative (values in splenic samples were set to 1) 2-NBDG expression ($n = 14$) in T_{reg} cells from the spleen and spinal cord of MOG-induced EAE mice on day 16 after MOG immunization. (**m**) *Scap* mRNA expression was examined in T_{reg}, naïve CD4$^+$, and CD8$^+$ T cells from *Foxp3*[Cre]*Scap*$^{+/fl}$ and *Foxp3*[Cre]*Scap*$^{fl/fl}$ mice under steady state ($n = 5$ samples per genotype). (**n**) Heat map of SREBP gene target expression normalized by row (z-score) in the tumour-infiltrating T_{reg} cells from B16 melanoma-bearing mice on day 19 after tumour inoculation ($n = 4$, *Foxp3*[Cre]*Scap*$^{+/+ \text{ or } +/fl}$ mice; $n = 3$, *Foxp3*[Cre]*Scap*$^{fl/fl}$ mice). (**o**) *Foxp3*[GFP-Cre-ERT2]*Scap*$^{+/fl}$*Rosa26*[YFP] and *Foxp3*[GFP-Cre-ERT2]*Scap*$^{fl/fl}$*Rosa26*[YFP] mice were injected with MC38 cells without tamoxifen treatment ($n = 6$ mice per genotype). Tumour growth was measured. ***P < 0.001, NS, not significant. Two-tailed unpaired Student's *t*-test (**k–m**) or two-way ANOVA (**o**). Data are mean ± s.e.m. in **d–g**, **j–m**, **o**. Data are representative of two (**o**), or compiled from two (**k, l**) independent experiments.
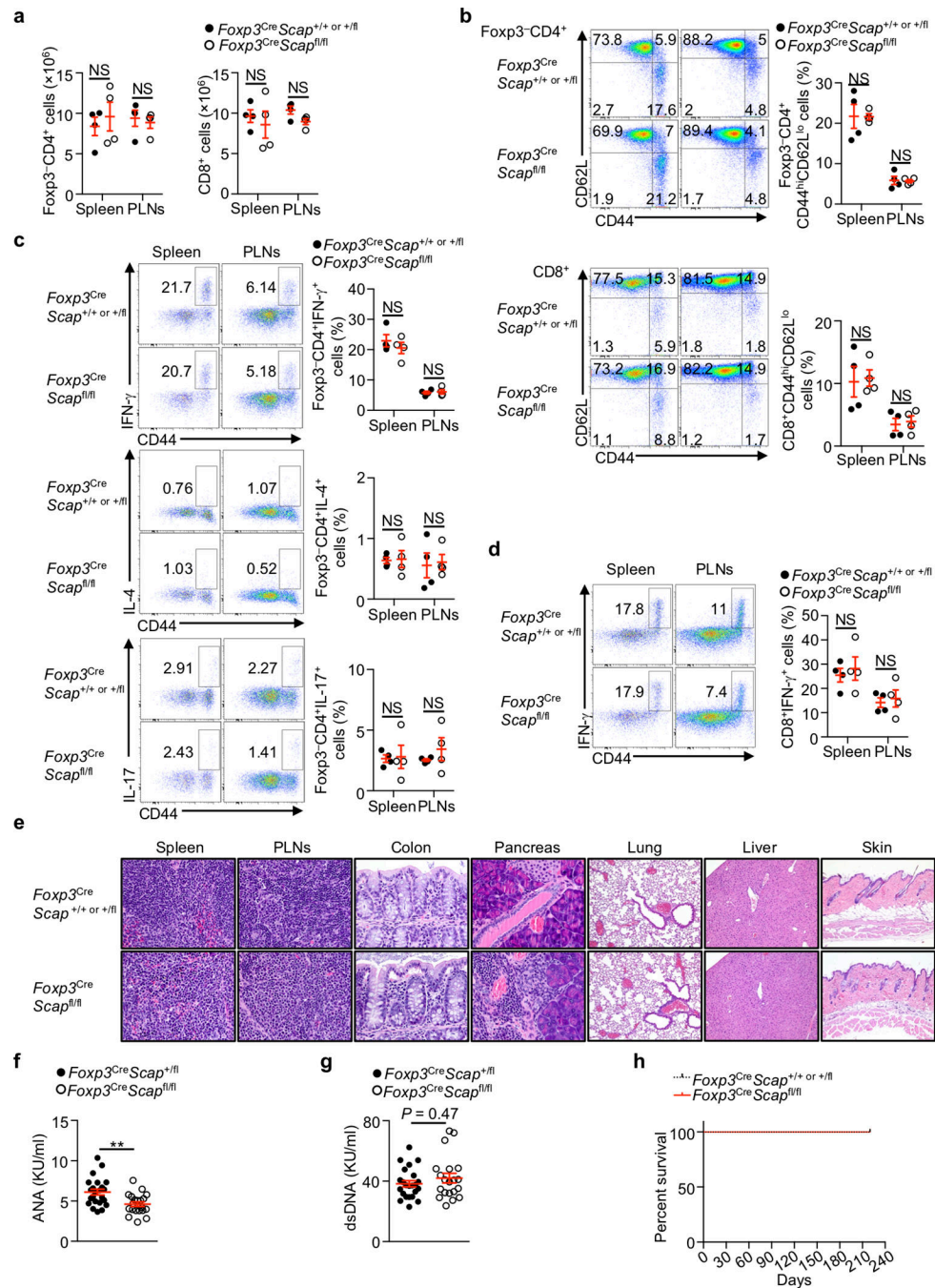
Extended Data Figure 2. SCAP is dispensable for T_reg cells to maintain immune homeostasis under steady state.

(**a**–**d**) Analyses of *Foxp3*^Cre *Scap*^+/+ or +/fl (*Foxp3*^Cre *Scap*^+/+ or *Foxp3*^Cre *Scap*^+/fl mice that were phenotypically indistinguishable) and *Foxp3*^Cre *Scap*^fl/fl mice (12–18 weeks) under steady state ($n = 4$ mice per genotype). (**a**) Cellularity of Foxp3⁻CD4⁺ and CD8⁺ T cells in spleen and PLNs. (**b**) Flow cytometry analysis of the expression of CD62L and CD44 (left) and quantification of the frequency of CD44^hiCD62L^lo cells (right) in Foxp3⁻CD4⁺ (upper) or CD8⁺ T cells (lower) from spleen and PLNs. (**c**) Flow cytometry analysis of the

expression of IFN-γ, IL-4 and IL-17 (left), and quantification of frequencies of IFN-γ^{+}, IL-4^{+} and IL-17^{+} cells (right) in Foxp3^{−}CD4^{+} T cells from spleen and PLNs. (**d**) Flow cytometry analysis of the expression of IFN-γ (left), and quantification of frequency of IFN-γ^{+} cells (right) in CD8^{+} T cells from spleen and PLNs. (**e**) Hematoxylin and eosin staining of spleen, PLNs, colon, pancreas, lung, liver, and skin from age-matched *Foxp3*[Cre]*Scap*[+/+ or +/fl] and *Foxp3*[Cre]*Scap*^{fl/fl} mice (28–35 weeks). (**f, g**) Quantification of anti-nuclear antibodies (ANAs) (**f**) and anti-dsDNA antibodies (**g**) in the serum of *Foxp3*[Cre]*Scap*^{+/fl} and *Foxp3*[Cre]*Scap*^{fl/fl} mice (> 3 months old) (*n* = 23, *Foxp3*[Cre]*Scap*^{+/fl} mice; *n* = 20, *Foxp3*[Cre]*Scap*^{fl/fl} mice). (**h**) Survival curve of *Foxp3*[Cre]*Scap*[+/+ or +/fl] (*n* = 17) and *Foxp3*[Cre]*Scap*^{fl/fl} mice (*n* = 27). **P < 0.01, NS, not significant. Two-tailed unpaired Student's *t*-test (**a**–**d**, **f**, **g**). Data are mean ± s.e.m. Data are compiled from two (**a**–**d**) independent experiments.
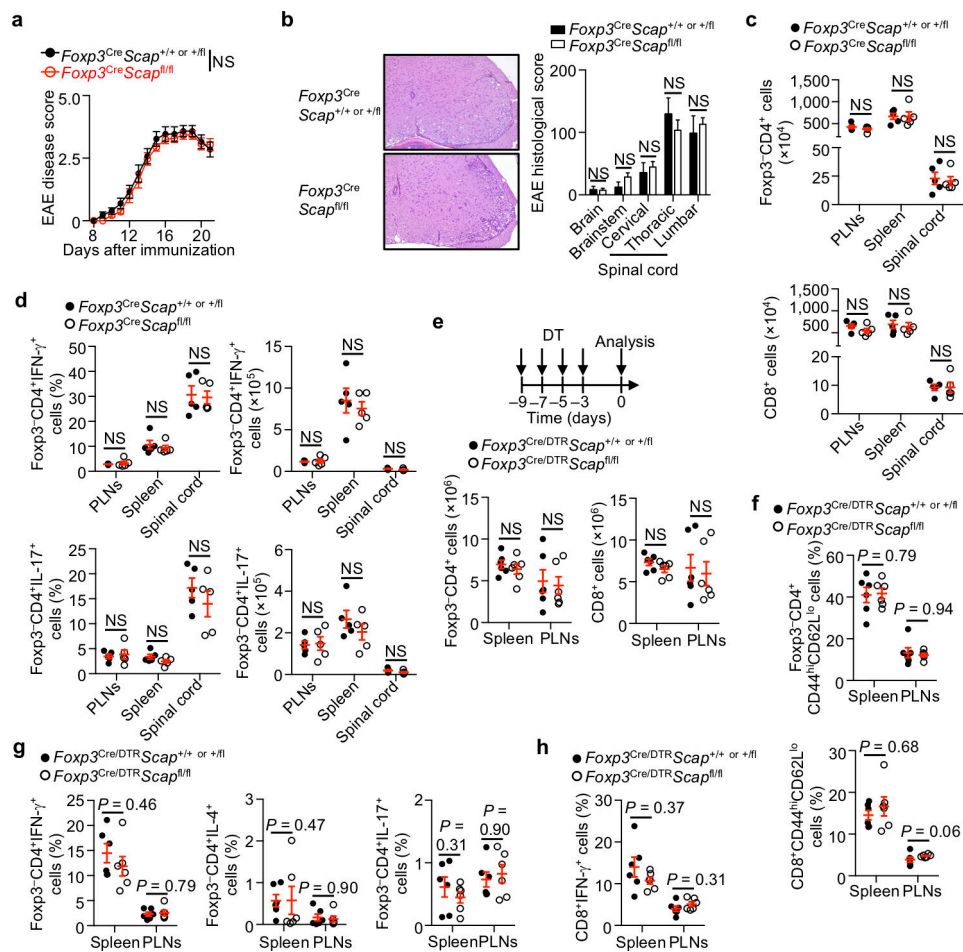
Extended Data Figure 3. SCAP is dispensable for T_reg cell function in autoimmune and acute inflammation.

(**a**) *Foxp3*[Cre]*Scap*[+/+ or +/fl] (*n* = 13) and *Foxp3*[Cre]*Scap*^{fl/fl} (*n* = 14) mice were immunized with MOG and EAE disease score was measured every day for 20 days. 0, no overt signs of disease; 1, limp tail; 2, limp tail plus hindlimb weakness; 3, total hindlimb paralysis; 4, hindlimb paralysis plus 75% of body paralysis (forelimb paralysis/weakness); 5, moribund.

(**b**) Mice as in (**a**) were sacrificed in the recovery phase (day 22–25) of EAE for histological analysis of clinical disease. Hematoxylin and eosin staining of the spinal cord (left) and the histological scores of the indicated regions of the brain and spinal cord (right) ($n = 9$, $Foxp3^{Cre}Scap^{+/+ \text{ or } +/fl}$ mice; $n = 10$, $Foxp3^{Cre}Scap^{fl/fl}$ mice). (**c, d**) $Foxp3^{Cre}Scap^{+/+ \text{ or } +/fl}$ and $Foxp3^{Cre}Scap^{fl/fl}$ mice were immunized with MOG to induce EAE ($n = 5$ mice per genotype) and sacrificed on day 16 for analysis. (**c**) Cellularity of Foxp3⁻CD4⁺ (upper) and CD8⁺ (lower) T cells in PLNs, spleen and spinal cord. (**d**) Quantification of percentages (left) and numbers (right) of IFN-γ⁺ (upper) and IL-17⁺ (lower) Foxp3⁻CD4⁺ T cells from PLNs, spleen and spinal cord. (**e–h**) $Foxp3^{Cre/DTR}Scap^{+/+ \text{ or } +/fl}$ and $Foxp3^{Cre/DTR}Scap^{fl/fl}$ mosaic mice were treated with diphtheria toxin (DT) (**e**, upper, for experimental design; $n = 6$ mice per genotype) and sacrificed 3 days after the final DT injection. (**e**) Quantification of cellularity of Foxp3⁻CD4⁺ (lower left) and CD8⁺ T cells (lower right). (**f**) Quantification of the frequency of CD44^hi CD62L^lo cells in Foxp3⁻CD4⁺ (upper) and CD8⁺ (lower) T cells from spleen and PLNs. (**g**) Quantification of frequencies of IFN-γ⁺ (left), IL-4⁺ (middle) and IL-17⁺ (right) cells in Foxp3⁻CD4⁺ T cells from spleen and PLNs. (**h**) Quantification of frequency of IFN-γ⁺ cells in CD8⁺ T cells from spleen and PLNs. NS, not significant. Two-tailed unpaired Student's *t*-test (**b–h**) or two-way ANOVA (**a**). Data are mean ± s.e.m. in **a–h**. Data are compiled from three (**a**) or two (**b, e–h**) independent experiments.
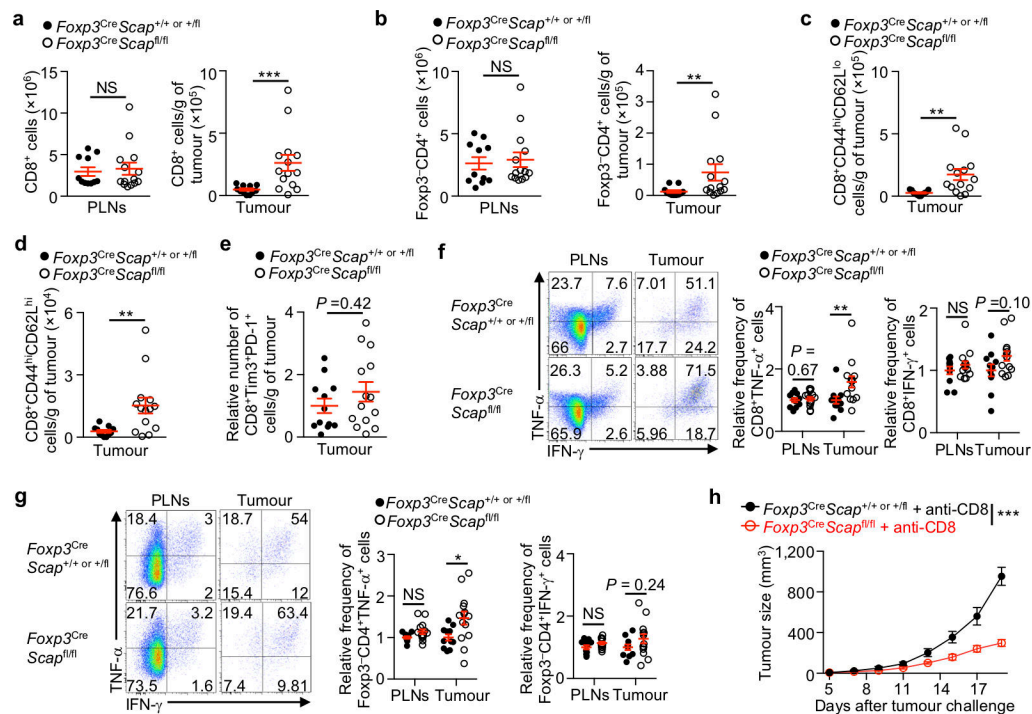
Extended Data Figure 4. SCAP/SREBP signalling maintains T_{reg} cell functional state in the TME.
(**a–d**) $Foxp3^{Cre}Scap^{+/+ \text{ or } +/fl}$ ($n = 11$) and $Foxp3^{Cre}Scap^{fl/fl}$ ($n = 14$) mice were inoculated with B16 cells. Cellularity of CD8⁺ T cells (gated as CD8α⁺TCRβ⁺) (**a**) and Foxp3⁻CD4⁺ T cells (**b**) in PLNs (left) and tumours (right; normalized to tumour weight to account for differences in tumour size between the genetic models) on day 19. (**c, d**) Quantification of numbers of CD44^hi CD62L^lo (T_{em}) cells (**c**) and CD44^hi CD62L^hi (T_{cm}) cells (**d**) in CD8⁺ T

cells from tumours. (**e**) *Foxp3*Cre*Scap*+/+ or +/fl ($n = 12$) and *Foxp3*Cre*Scap*fl/fl ($n = 14$) mice were inoculated with B16 cells. Quantification of number of Tim3+PD-1+ (T_{ex}) cells in CD8+ T cells from tumours. (**f, g**) *Foxp3*Cre*Scap*+/+ or +/fl ($n = 11$) and *Foxp3*Cre*Scap*fl/fl ($n = 14$) mice were inoculated with B16 cells. Flow cytometry analysis of the expression of TNF-α and IFN-γ (left), and relative frequency of TNF-α+ cells (middle) and IFN-γ+ cells (right) in CD8+ T cells (**f**) and Foxp3−CD4+ T cells (**g**) from PLNs and tumours. (**h**) *Foxp3*Cre*Scap* +/+ or +/fl and *Foxp3*Cre*Scap*fl/fl mice were inoculated with MC38 cells on day 0 and treated with anti-CD8 on days 1, 2, 5, 8 and 11. Tumour growth was measured ($n = 6$ mice per genotype). *$P< 0.05$, **$P< 0.01$, ***$P< 0.001$, NS, not significant. Two-tailed unpaired Student's t-test (**a**–**g**) or two-way ANOVA (**h**). Data are mean ± s.e.m. in **a**–**h**. Data are representative of two (**h**), or compiled from two (**a**–**g**) independent experiments.
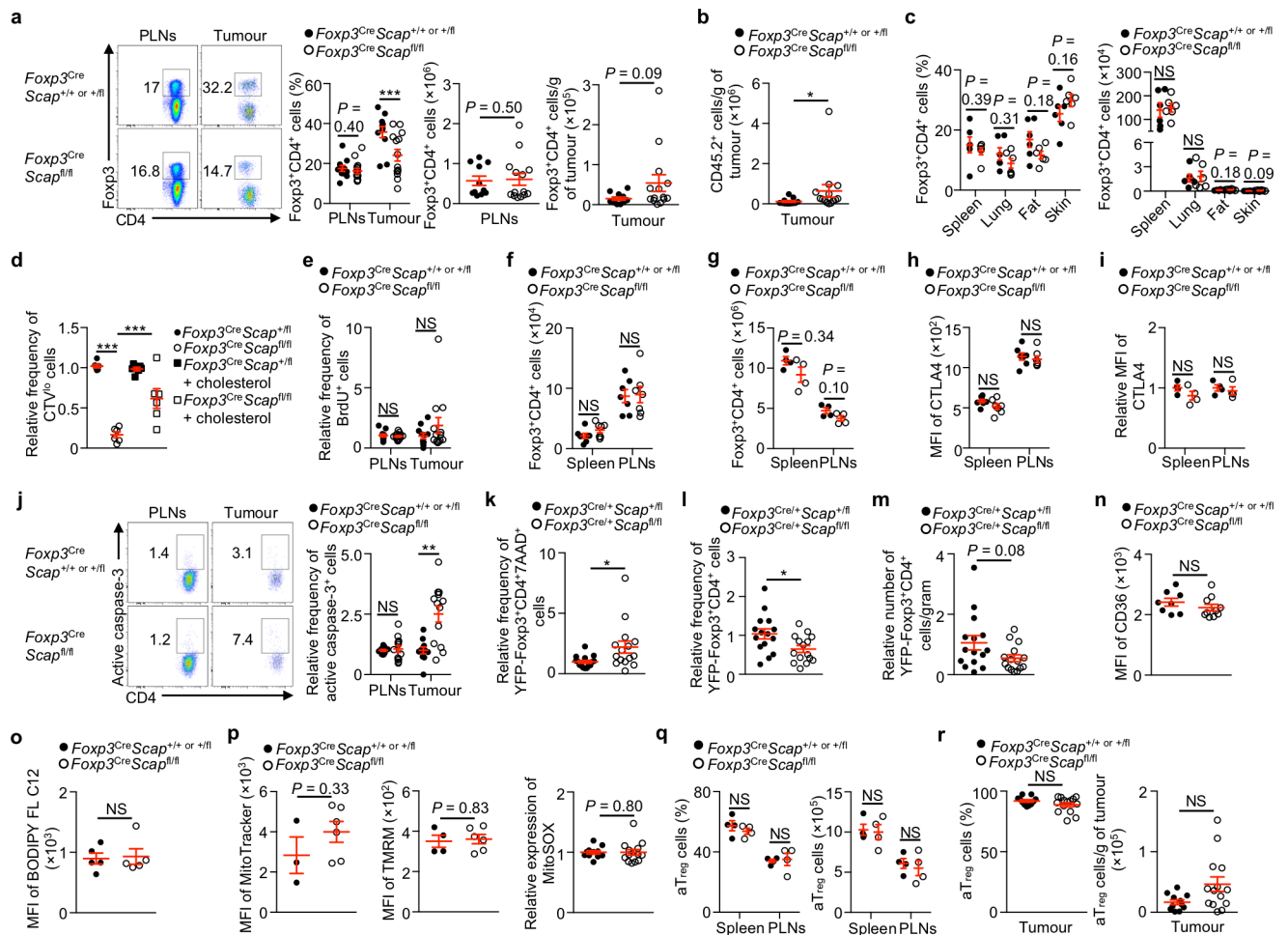
Extended Data Figure 5. *Scap*-deficient T_{reg} cellular state in tumours and homeostasis.
(**a**) *Foxp3*Cre*Scap*+/+ or +/fl and *Foxp3*Cre*Scap*fl/fl mice were inoculated with B16 melanoma cells and sacrificed on day 19. Flow cytometry analysis (left panel) and quantification of frequency (second panel) and number (third panel shows raw values of cell number; right panel shows cell number normalized to tumour weight) of Foxp3+CD4+ T cells in PLNs and tumours ($n = 11$, *Foxp3*Cre*Scap*+/+ or +/fl mice; $n = 14$, *Foxp3*Cre*Scap*fl/fl mice). (**b**) Quantification of number of CD45.2+ cells from B16 melanoma-bearing *Foxp3*Cre*Scap*

+/+ or +/fl control ($n = 11$) and $Foxp3^{Cre}Scap^{fl/fl}$ ($n = 14$) mice. (**c**) Quantification of frequency (left) and number (right) of Foxp3$^+$CD4$^+$ T$_{reg}$ cells in spleen, lung, fat tissue and skin in $Foxp3^{Cre}Scap^{+/+ \text{ or } +/fl}$ control and $Foxp3^{Cre}Scap^{fl/fl}$ mice under steady state ($n = 6$ mice per genotype). (**d**) Foxp3-YFP$^+$CD4$^+$ cells were sorted from $Foxp3^{Cre}Scap^{+/fl}$ and $Foxp3^{Cre}Scap^{fl/fl}$ mice, labelled with CellTrace Violet (CTV), and cultured with anti-CD3/28 antibodies plus IL-2 for 3 days. T$_{reg}$ cells were pre-treated with cholesterol for 1 h or vehicle before activation ($n = 6$ per group). Relative frequency of CTV^{lo} cells. (**e**) $Foxp3^{Cre}Scap^{+/+ \text{ or } +/fl}$ control ($n = 11$) and $Foxp3^{Cre}Scap^{fl/fl}$ ($n = 13$) mice were inoculated with B16 cells. Relative frequency of BrdU$^+$ cells among Foxp3$^+$CD4$^+$ T$_{reg}$ cells from PLNs and tumours. (**f**) T$_{reg}$ cells from $Foxp3^{Cre}Scap^{+/+ \text{ or } +/fl}$ control and $Foxp3^{Cre}Scap^{fl/fl}$ mice were labelled with CTV and transferred into $Rag1^{-/-}$ mice. Mice were sacrificed on day 10 for analysis. Quantification of cellularity of Foxp3$^+$CD4$^+$ T$_{reg}$ cells in spleen and PLNs ($n = 7$ mice per genotype). (**g**) $Foxp3^{Cre}Scap^{+/+ \text{ or } +/fl}$ control and $Foxp3^{Cre}Scap^{fl/fl}$ mice received *i.p.* injection of IL-2/anti-IL-2 complex daily on days 0–2 to induce T$_{reg}$ cell expansion[19], and analyzed on day 5. Quantification of number of Foxp3$^+$CD4$^+$ T$_{reg}$ cells in spleen and PLNs ($n = 4$ mice per genotype). (**h**) T$_{reg}$ cells from $Foxp3^{Cre}Scap^{+/+ \text{ or } +/fl}$ control and $Foxp3^{Cre}Scap^{fl/fl}$ mice were transferred into $Rag1^{-/-}$ recipients and analyzed as in (**f**). Quantification of mean fluorescence intensity (MFI) of CTLA4 in T$_{reg}$ cells ($n = 7$ mice per genotype) from spleen and PLNs. (**i**) Relative MFI of CTLA4 in T$_{reg}$ cells from IL-2/anti-IL-2 complex-treated $Foxp3^{Cre}Scap^{+/+ \text{ or } +/fl}$ control and $Foxp3^{Cre}Scap^{fl/fl}$ mice ($n = 4$ mice per genotype) as in (**g**). (**j**) $Foxp3^{Cre}Scap^{+/+ \text{ or } +/fl}$ and $Foxp3^{Cre}Scap^{fl/fl}$ mice were inoculated with B16 melanoma cells and sacrificed on day 19. Flow cytometry analysis (left) and relative frequency (right) of active caspase-3$^+$ T$_{reg}$ cells from PLNs and tumours ($n = 11$, $Foxp3^{Cre}Scap^{+/+ \text{ or } +/fl}$ control mice; $n = 13$, $Foxp3^{Cre}Scap^{fl/fl}$ mice). (**k–m**) Female $Foxp3^{Cre/+}Scap^{+/fl}$ control and $Foxp3^{Cre/+}Scap^{fl/fl}$ mosaic mice were challenged with B16 cells and sacrificed on day 14 ($n = 15$ mice per genotype). (**k**) Relative frequency of 7AAD$^+$ cells in Foxp3$^+$CD4$^+$ T$_{reg}$ cells from tumours. (**l**) Relative frequency of Foxp3$^+$CD4$^+$ T$_{reg}$ cells from tumours. (**m**) Relative number of Foxp3$^+$CD4$^+$ T$_{reg}$ cells from tumours. (**n–p**) $Foxp3^{Cre}Scap^{+/+ \text{ or } +/fl}$ control and $Foxp3^{Cre}Scap^{fl/fl}$ mice were inoculated with B16 cells and sacrificed on day 19. CD36 expression ($n = 8$, $Foxp3^{Cre}Scap^{+/+ \text{ or } +/fl}$ mice; $n = 10$, $Foxp3^{Cre}Scap^{fl/fl}$ mice) (**n**), uptake of BODIPY FL C12 ($n = 5$ mice per genotype) (**o**), MitoTracker ($n = 3$, $Foxp3^{Cre}Scap^{+/+ \text{ or } +/fl}$ mice; $n = 6$, $Foxp3^{Cre}Scap^{fl/fl}$ mice) (**p**, left), TMRM expression ($n = 4$, $Foxp3^{Cre}Scap^{+/+ \text{ or } +/fl}$ mice; $n = 6$, $Foxp3^{Cre}Scap^{fl/fl}$ mice) (**p**, middle) and MitoSOX expression ($n = 11$, $Foxp3^{Cre}Scap^{+/+ \text{ or } +/fl}$ mice; $n = 14$, $Foxp3^{Cre}Scap^{fl/fl}$ mice) (**p**, right) in T$_{reg}$ cells. (**q**) Quantification of the frequency (left) and number (right) of CD44^{hi}CD62L^{lo} aT$_{reg}$ cells among Foxp3$^+$CD4$^+$ T$_{reg}$ cells from spleen and PLNs under steady state ($n = 4$ mice per genotype). (**r**) Quantification of frequency (left) and number of aT$_{reg}$ cells in tumours (right; normalized to tumour weight) from $Foxp3^{Cre}Scap^{+/+ \text{ or } +/fl}$ control ($n = 11$) and $Foxp3^{Cre}Scap^{fl/fl}$ ($n = 14$) mice challenged with B16 cells. * $P < 0.05$, **$P < 0.01$, *** $P < 0.001$, NS, not significant. Two-tailed unpaired Student's *t*-test (**a–c, e–r**) and one-way ANOVA (**d**). Data are mean ± s.e.m. in **a–r**. Data are representative of two (**f**; **h**; **o**; **p**, left, middle), or compiled from three (**d, e, j**) or two (**a–c**; **g**; **i**; **k–n**; **p**, right; **q**; **r**) independent experiments. Values in control samples were set to 1 (**d**; **e**; **i**; **j**; **k–m**; **p**, right).
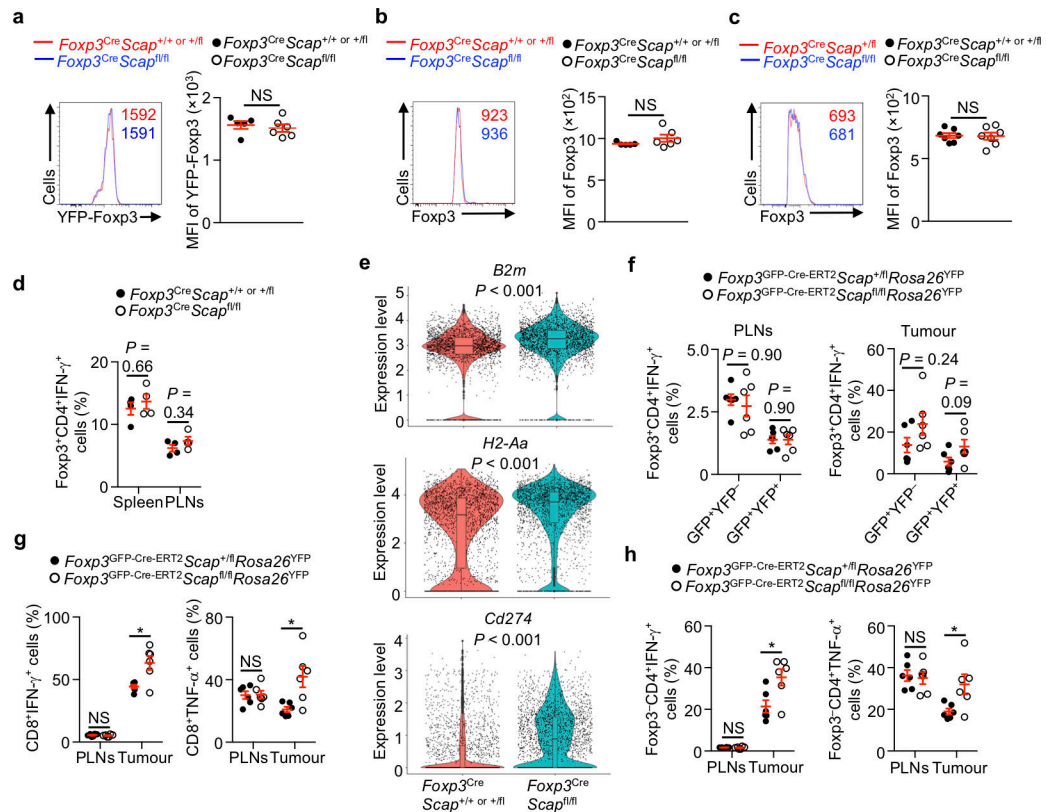
Extended Data Figure 6. *Scap*-deficient T_{reg} functional integrity in tumours and homeostasis.
(**a**) Flow cytometry analysis (left) and quantification of the mean fluorescence intensity (MFI) of Foxp3-YFP (right) in intratumoural T_{reg} cells from B16 melanoma-bearing *Foxp3*^{Cre}*Scap*$^{+/+ \text{ or } +/fl}$ control (*n* = 5) and *Foxp3*^{Cre}*Scap*$^{fl/fl}$ (*n* = 6) mice. (**b**) Flow cytometry analysis (left) and quantification of the MFI (right) of Foxp3 protein in intratumoural T_{reg} cells from B16 melanoma-bearing *Foxp3*^{Cre}*Scap*$^{+/+ \text{ or } +/fl}$ control (*n* = 5) and *Foxp3*^{Cre}*Scap*$^{fl/fl}$ (*n* = 6) mice. (**c**) Flow cytometry analysis (left) and quantification of the MFI (right) of Foxp3 protein in T_{reg} cells (from *Foxp3*^{Cre}*Scap*$^{+/fl}$ control and *Foxp3*^{Cre}*Scap*$^{fl/fl}$ mice) transferred into *Rag1*$^{-/-}$ recipients (*n* = 7 mice per genotype). (**d**) Quantification of frequency of IFN-γ^+ cells in Foxp3$^+$CD4$^+$ T_{reg} cells in spleen and PLNs from *Foxp3*^{Cre}*Scap*$^{+/+ \text{ or } +/fl}$ control and *Foxp3*^{Cre}*Scap*$^{fl/fl}$ mice under steady state (*n* = 4 mice per genotype). (**e**) Violin plots of gene expression in macrophages from scRNA-seq analysis of tumour-infiltrating CD45$^+$ cells in mice challenged with B16 melanoma cells (*n* = 2 mice per genotype; see also Fig. 2a). (**f**–**h**) *Foxp3*$^{GFP-Cre-ERT2}$*Scap*$^{+/fl}$*Rosa26*^{YFP} and *Foxp3*$^{GFP-Cre-ERT2}$*Scap*$^{fl/fl}$*Rosa26*^{YFP} mice were injected with MC38 colon adenocarcinoma cells on day 0, treated with tamoxifen daily on days 7–11 (*n* = 6 mice per genotype), and analyzed on day 21 after tumour injection. (**f**) Quantification of the frequencies of IFN-γ^+ cells among GFP$^+$YFP$^-$ and GFP$^+$YFP$^+$ T_{reg} cells from PLNs (left) and tumours (right). (**g**) Quantification of frequencies of IFN-γ^+ (left) and TNF-α^+ (right) cells among CD8$^+$ T cells in PLNs and tumours. (**h**) Quantification of frequencies of IFN-γ^+ (left) and TNF-α^+ (right) cells among Foxp3$^-$CD4$^+$ T cells in PLNs and tumours. *P < 0.05, NS, not significant. Two-tailed unpaired Student's *t*-test (**a**–**d**, **f**–**h**). Data are mean ± s.e.m. in **a**–**h**. Data are representative of two (**a**–**c**), or compiled from two (**d**) independent experiments.
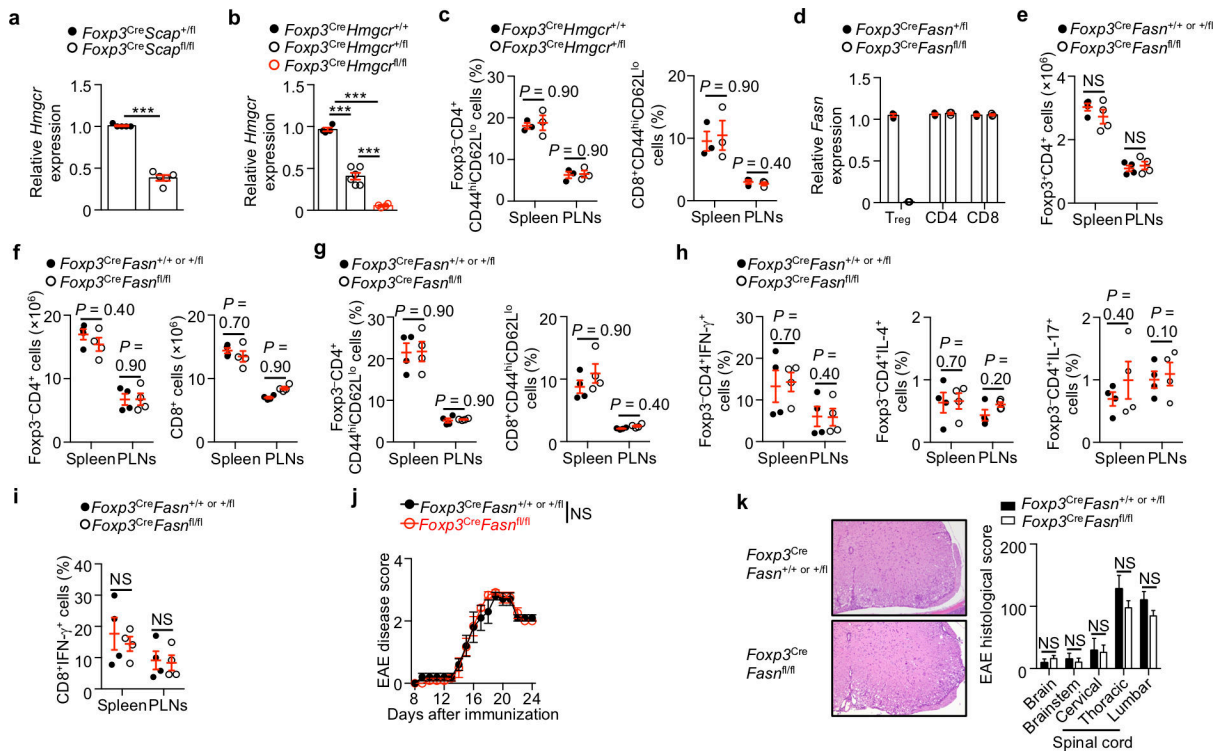
Extended Data Figure 7. FASN is dispensable for T_{reg} cell function in steady state and autoimmunity.
(**a**) *Hmgcr* mRNA expression was examined in T_{reg} cells from *Foxp3*^{Cre}*Scap*$^{+/fl}$ and *Foxp3*^{Cre}*Scap*$^{fl/fl}$ mice under steady state ($n = 5$ samples per genotype). (**b**) *Hmgcr* mRNA expression was examined in T_{reg} cells from *Foxp3*^{Cre}*Hmgcr*$^{+/+}$ ($n = 4$), *Foxp3*^{Cre}*Hmgcr*$^{+/fl}$ ($n = 6$), and *Foxp3*^{Cre}*Hmgcr*$^{fl/fl}$ ($n = 4$) mice under steady state. (**c**) Analyses of T cell homeostasis in *Foxp3*^{Cre}*Hmgcr*$^{+/+}$ and *Foxp3*^{Cre}*Hmgcr*$^{+/fl}$ mice (6–10 weeks; $n = 3$ mice per genotype). Quantification of the frequency of CD44^{hi}CD62L^{lo} cells in Foxp3$^-$CD4$^+$ (left) and CD8$^+$ T cells (right) from spleen and PLNs. (**d**) *Fasn* mRNA expression was examined in T_{reg}, naïve CD4$^+$, and CD8$^+$ T cells from *Foxp3*^{Cre}*Fasn*$^{+/fl}$ and *Foxp3*^{Cre}*Fasn*$^{fl/fl}$ mice under steady state ($n = 3$ samples per genotype). (**e–i**) Analysis of spleen and PLNs from *Foxp3*^{Cre}*Fasn*$^{+/+ or +/fl}$ control and *Foxp3*^{Cre}*Fasn*$^{fl/fl}$ mice (8–12 weeks) under steady state ($n = 4$ mice per genotype). Quantification of numbers of Foxp3$^+$CD4$^+$ T_{reg} cells (**e**) and Foxp3$^-$CD4$^+$ (**f**, left) and CD8$^+$ (**f**, right) T cells. (**g**) Quantification of frequencies of CD44^{hi}CD62L^{lo} cells in Foxp3$^-$CD4$^+$ (left) and CD8$^+$ (right) T cells. (**h**) Quantification of frequencies of IFN-γ^+ (left), IL-4$^+$ (middle) and IL-17$^+$ (right) cells among Foxp3$^-$CD4$^+$ T cells. (**i**) Quantification of frequency of IFN-γ^+ cells among CD8$^+$ T cells. (**j**) *Foxp3*^{Cre}*Fasn*$^{+/+ or +/fl}$ ($n = 5$) and *Foxp3*^{Cre}*Fasn*$^{fl/fl}$ ($n = 6$) mice were immunized with MOG and EAE disease score was measured every day until day 24. (**k**) Mice as in (**j**) were sacrificed in the recovery phase (day 24) of EAE for histological analysis of clinical disease. Hematoxylin and eosin staining of the spinal cord (left) and the histological scores of the indicated regions of the brain and spinal cord (right) ($n = 5$, *Foxp3*^{Cre}*Fasn*$^{+/+ or +/fl}$ mice; $n = 6$, *Foxp3*^{Cre}*Fasn*$^{fl/fl}$ mice). ***$P < 0.001$, NS, not significant. Two-tailed unpaired Student's *t*-

test (**a**, **c**–**i**, **k**), one-way ANOVA (**b**), or two-way ANOVA (**j**). Data are mean ± s.e.m. in **a**–**k**. Data are compiled from two (**e**–**i**) independent experiments.
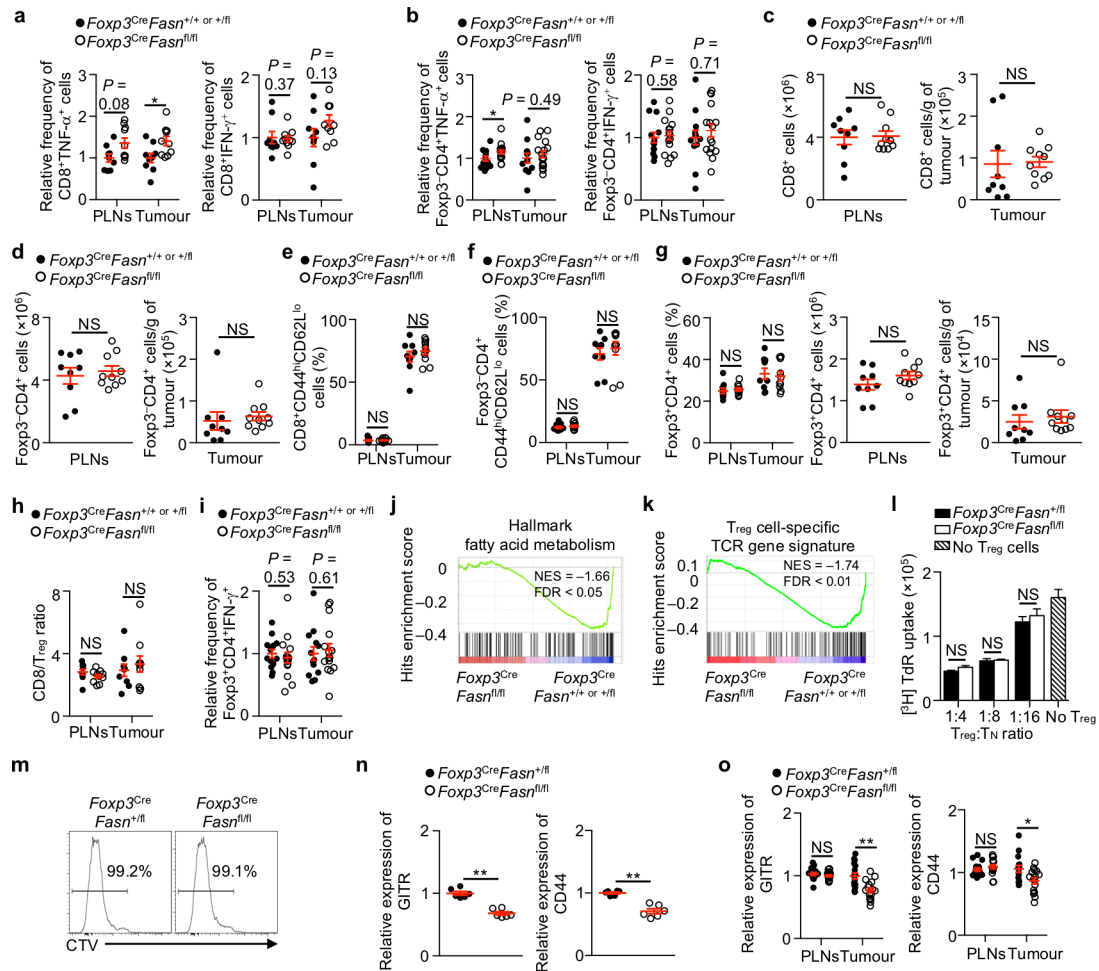
Extended Data Figure 8. Antitumour response of $Foxp3^{Cre}Fasn^{fl/fl}$ mice.
(**a**, **b**) $Foxp3^{Cre}Fasn^{+/+ \text{ or } +/fl}$ control (**a**, $n = 9$; **b**, $n = 13$) and $Foxp3^{Cre}Fasn^{fl/fl}$ (**a**, $n = 10$; **b**, $n = 16$) bone marrow chimeras were inoculated with B16 cells and sacrificed on day 17 (**a**) or days 17–19 (**b**). Relative frequencies of TNF-α^+ cells (left) and IFN-γ^+ cells (right) among $CD8^+$ T cells (**a**) and $Foxp3^-CD4^+$ T cells (**b**). (**c**–**h**) $Foxp3^{Cre}Fasn^{+/+ \text{ or } +/fl}$ control ($n = 9$) and $Foxp3^{Cre}Fasn^{fl/fl}$ ($n = 10$) bone marrow chimeras were inoculated with B16 cells and sacrificed on day 17. (**c**, **d**) Quantification of numbers of $CD8^+$ T cells (**c**) and $Foxp3^-CD4^+$ T cells (**d**) in PLNs (left) and tumours (right; normalized to tumour weight). (**e**, **f**) Quantification of frequency of $CD44^{hi}CD62L^{lo}$ cells in $CD8^+$ T cells (**e**) and $Foxp3^-CD4^+$ T cells (**f**). (**g**) Quantification of frequency (left) and number of $Foxp3^+CD4^+$ T cells in PLNs (middle) and tumours (right; normalized to tumour weight). (**h**) Quantification of $CD8/T_{reg}$ cell ratio. (**i**) $Foxp3^{Cre}Fasn^{+/+ \text{ or } +/fl}$ control ($n = 13$) and $Foxp3^{Cre}Fasn^{fl/fl}$ ($n = 16$) bone marrow chimeras were inoculated with B16 cells and sacrificed on days 17–19. Relative frequency of IFN-γ^+ cells among $Foxp3^+CD4^+$ T_{reg} cells in PLNs and tumours. (**j**, **k**) GSEA enrichment plots of fatty acid metabolism (**j**) and T_{reg} cell-specific TCR gene signature

(genes downregulated in TCRα-deficient aT$_{reg}$ cells compared to TCRα-sufficient aT$_{reg}$ cells) (**k**) in intratumoural T$_{reg}$ cells from B16 melanoma-bearing *Foxp3*^{Cre}*Fasn*$^{+/+ \text{ or } +/fl}$ and *Foxp3*^{Cre}*Fasn*$^{fl/fl}$ mice ($n = 3$ samples per genotype). (**l**) T$_{reg}$ cells from *Foxp3*^{Cre}*Fasn*$^{+/fl}$ control and *Foxp3*^{Cre}*Fasn*$^{fl/fl}$ mice were used for *in vitro* suppression assays at multiple T$_{reg}$ versus T$_N$ (naïve CD4$^+$ T cell) ratios. (**m, n**) T$_{reg}$ cells from control *Foxp3*^{Cre}*Fasn*$^{+/fl}$ and *Foxp3*^{Cre}*Fasn*$^{fl/fl}$ mice were labelled with CellTrace Violet (CTV), and cultured with anti-CD3/28 antibodies plus IL-2 for 3 days. Flow cytometry analysis for frequency of CTV^{lo} cells (**m**) and relative expression of GITR (**n**, left) and CD44 (**n**, right) ($n = 6$ per genotype). (**o**) Relative expression of GITR ($n = 16$ per genotype) (**o**, left) and CD44 ($n = 15$ per genotype) (**o**, right) on T$_{reg}$ cells in PLNs and tumours of B16 melanoma-bearing mice. *$P <$ 0.05, **$P <$ 0.01, NS, not significant. Two-tailed unpaired Student's *t*-test (**a–i, l, n, o**). Data are mean ± s.e.m. in **a–i, l, n, o**. Data are representative of four (**m**) or two (**l**), or compiled from three (**b, i**) or two (**a, c–h, n, o**) independent experiments. Values in control samples were set to 1 (**a, b, i, n, o**).
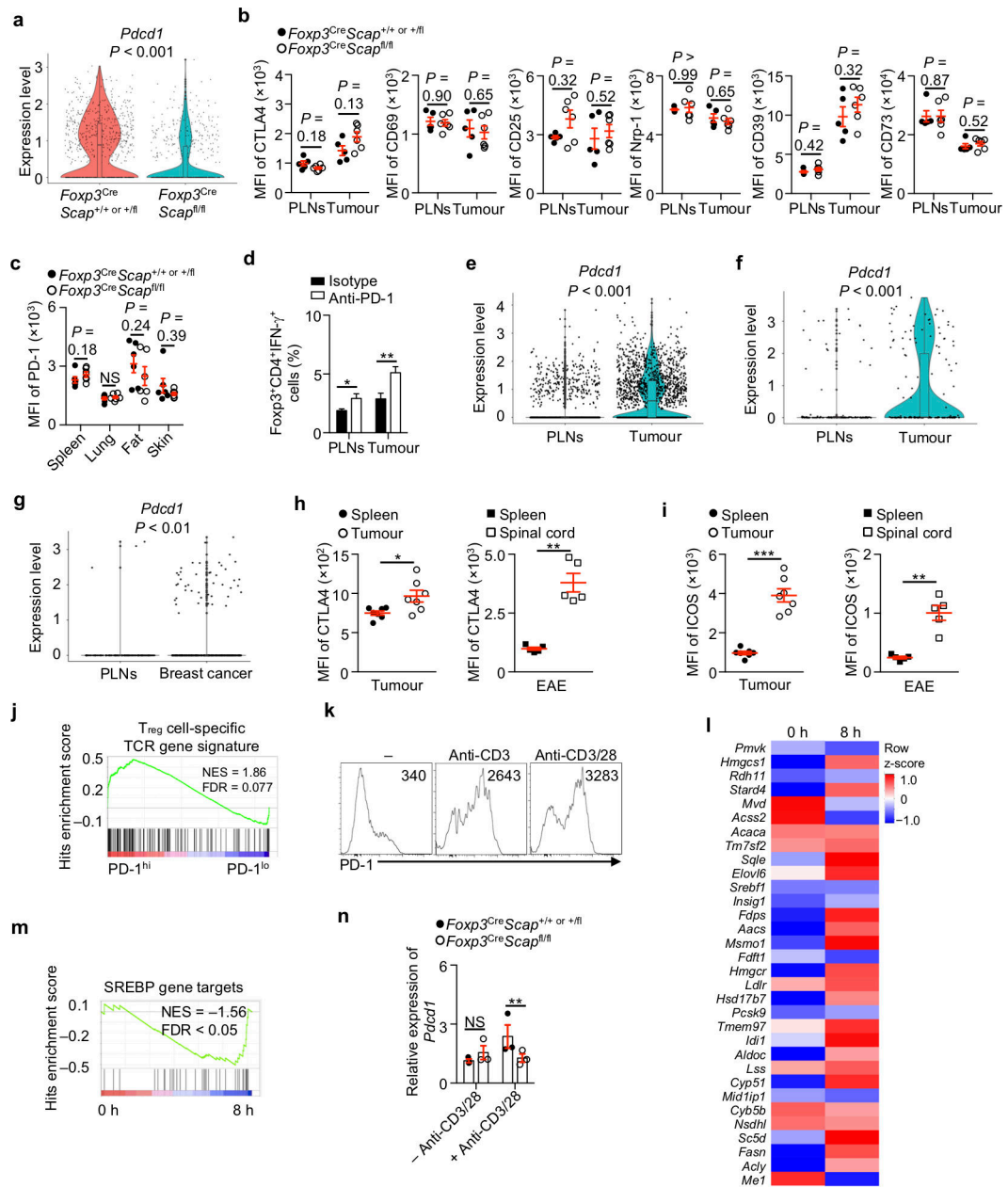
Extended Data Figure 9. SCAP/SREBP signalling promotes T_reg cell PD-1 expression in the TME and upon TCR stimulation.

(**a**) Violin plot of *Pdcd1* expression in T_reg cells from scRNA-seq analysis of tumour-infiltrating CD45$^+$ cells in mice challenged with B16 cells ($n = 2$ samples per genotype; see also Fig. 2a). (**b**) Quantification of mean fluorescence intensity (MFI) of CTLA4, CD69, CD25, Nrp-1, CD39 and CD73 on Foxp3$^+$CD4$^+$ T_reg cells in PLNs and tumours from *Foxp3*^{Cre}*Scap*$^{+/+ or +/fl}$ control ($n = 5$) and *Foxp3*^{Cre}*Scap*$^{fl/fl}$ ($n = 6$) mice challenged with B16 melanoma cells. (**c**) Quantification of PD-1 MFI in Foxp3$^+$CD4$^+$ T_reg cells in spleen, lung, fat tissue and skin from *Foxp3*^{Cre}*Scap*$^{+/+ or +/fl}$ and *Foxp3*^{Cre}*Scap*$^{fl/fl}$ mice under steady state ($n = 6$ mice per genotype). (**d**) C57BL/6 mice were inoculated with MC38 cells on day 0 and treated with either anti-PD-1 ($n = 8$) or isotype control ($n = 10$) antibody on

days 7, 10, and 13. Mice were sacrificed on day 14, and frequency of IFN-γ^+ cells in Foxp3$^+$CD4$^+$ T cells in PLNs and tumours were analyzed by flow cytometry and quantified. (**e**–**g**) Violin enrichment plot of *Pdcd1* expression from public scRNA-seq datasets from the mouse model of B16 melanoma tumours[7,8] (**e**, **f**) and human patients with breast cancer[9] (**g**). (**h**, **i**) Quantification of CTLA4 (**h**) and ICOS (**i**) MFIs in T$_{reg}$ cells from spleen and tumours in MC38 colon adenocarcinoma tumour-bearing mice (left panels; $n = 7$) or from spleen and spinal cord in MOG-induced EAE mice (right panels; $n = 5$). (**j**) Enrichment plot of T$_{reg}$ cell-specific TCR gene signature in transcriptome analysis of intratumoural PD-1^{hi} and PD-1^{lo} T$_{reg}$ cells from MC38 tumour-bearing mice. (**k**) Flow cytometry analysis of PD-1 expression on T$_{reg}$ cells cultured in the presence of IL-2 with or without anti-CD3 or anti-CD3/28 antibody stimulation for 3 days. Numbers in graphs indicate MFI. (**l**) Heat map of SREBP gene target expression normalized by row (z-score) in transcriptome analysis of T$_{reg}$ cells (from *Foxp3*^{Cre} mice) stimulated with anti-CD3/28 antibodies for 0 h and 8 h ($n = 5$ per time point). (**m**) Enrichment plot of SREBP gene targets in transcriptome analysis of T$_{reg}$ cells (from *Foxp3*^{Cre} mice) stimulated with anti-CD3/28 antibodies for 0 h and 8 h. (**n**) Real-time PCR analysis of *Pdcd1* mRNA expression in T$_{reg}$ cells from *Foxp3*^{Cre}*Scap*$^{+/+ \text{ or } +/fl}$ control and *Foxp3*^{Cre}*Scap*$^{fl/fl}$ mice ($n = 3$ samples per genotype) with or without anti-CD3/28 stimulation for 72 h. *$P < 0.05$, **$P < 0.01$, ***$P < 0.001$, NS, not significant. Two-tailed unpaired Student's *t*-test (**b**–**d**, **h**, **i**, **n**). Data are mean ± s.e.m. in **a**–**j**, **m**, **n**. Data are representative of two (**d**, **h**, **i**), or compiled from two (**c**) independent experiments.
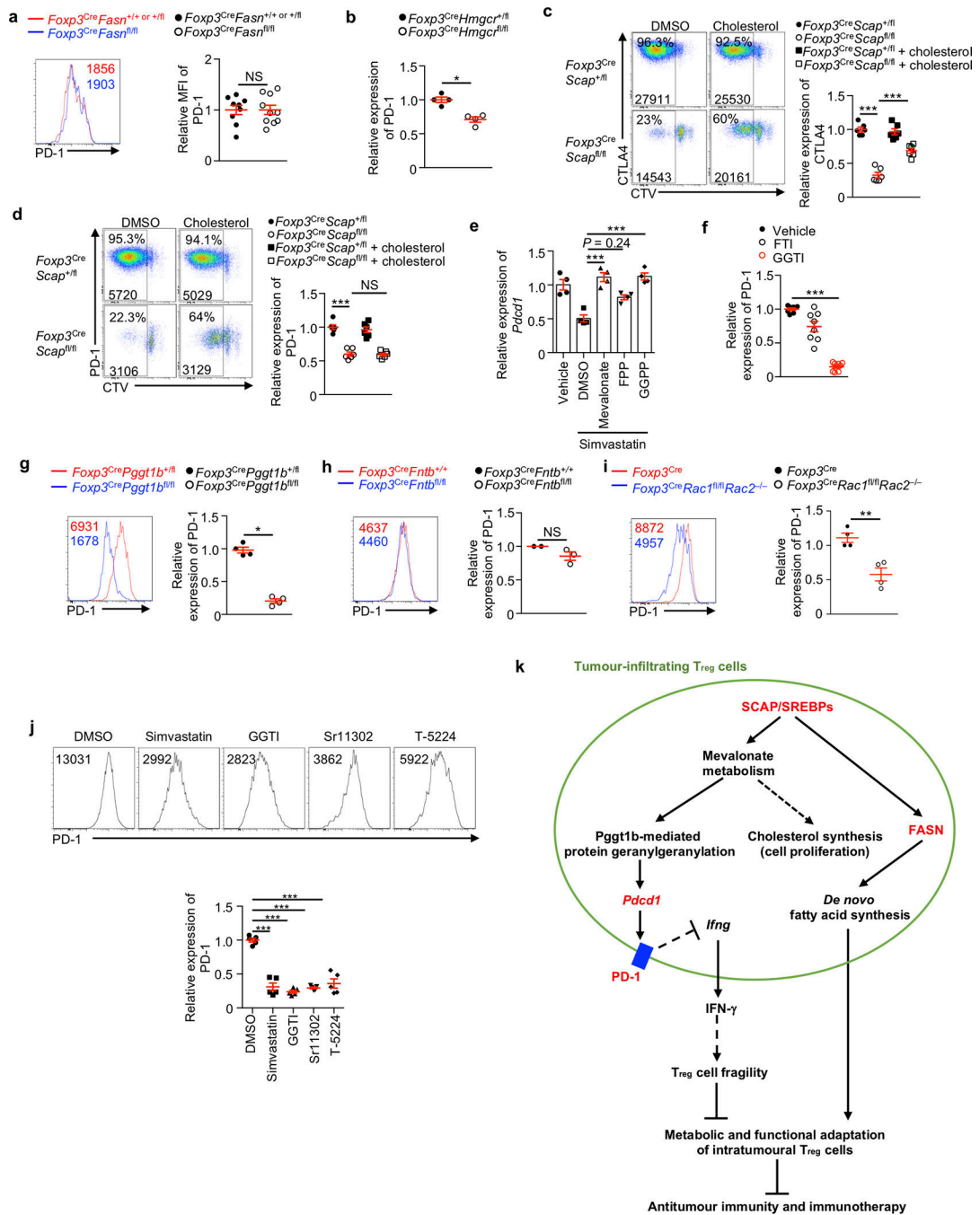
Extended Data Figure 10. Metabolic dependence of PD-1 expression on intratumoural T_reg cells and model of metabolic adaptation.

(**a**) Flow cytometry analysis (left) and quantification of relative mean fluorescence intensity (MFI) (right) of PD-1 on intratumoural T_reg cells from B16 melanoma-bearing *Foxp3*^Cre*Fasn*^+/+ or +/fl ($n = 9$) and *Foxp3*^Cre*Fasn*^fl/fl ($n = 10$) mice on day 17. (**b**) Resting T_reg cells were sorted from *Foxp3*^Cre*Hmgcr*^+/fl control and *Foxp3*^Cre*Hmgcr*^fl/fl mice under steady state ($n = 4$ samples per genotype), labelled with CellTrace Violet (CTV), and cultured with anti-CD3/28 antibodies plus IL-2 for 3 days. Relative MFI of PD-1 on CTV^lo

cells. (**c, d**) Foxp3-YFP$^+$CD4$^+$ cells were sorted from $Foxp3^{Cre}Scap^{+/fl}$ control and $Foxp3^{Cre}Scap^{fl/fl}$ mice, labelled with CTV, and cultured with anti-CD3/28 antibodies plus IL-2 for 3 days. T$_{reg}$ cells were pre-treated with cholesterol or vehicle for 1 h before activation ($n = 6$ samples per group). Flow cytometry analysis (left) and quantification of relative MFI (right) of CTLA4 (**c**) and PD-1 (**d**) in CTV^{lo} cells. (**e**) Foxp3-YFP$^+$CD4$^+$ cells were sorted from $Foxp3^{Cre}$ mice, treated with vehicle or simvastatin (2 μM), and then stimulated with anti-CD3/28 antibodies plus IL-2 for 18 h in the presence of mevalonate (500 μM), FPP (50 μM), GGPP (5 μM) or DMSO for real-time PCR analysis of $Pdcd1$ mRNA expression ($n = 4$). (**f**) T$_{reg}$ cells from $Foxp3^{Cre}$ mice were labelled with CTV and pre-treated with vehicle, FTI-277 (FTI) (10 μM), or GGTI-2147 (GGTI) (5 μM) for 1 h and then stimulated with anti-CD3/28 antibodies plus IL-2 for 72 h. Relative MFI of PD-1 on CTV^{lo} cells ($n = 8$ per group). (**g**) Resting T$_{reg}$ cells were sorted from young (1–3 weeks) $Foxp3^{Cre}Pggt1b^{+/fl}$ control and $Foxp3^{Cre}Pggt1b^{fl/fl}$ mice ($n = 4$ samples per genotype) under steady state; young mice were used to limit the influence of systemic inflammation. T$_{reg}$ cells were labelled with CTV and cultured with anti-CD3/28 antibodies plus IL-2 for 3 days. Flow cytometry analysis (left) and relative MFI (right) of PD-1 on CTV^{lo} cells. (**h**) Resting T$_{reg}$ cells were sorted from young (1–3 weeks) $Foxp3^{Cre}Fntb^{+/+}$ control ($n = 2$) and $Foxp3^{Cre}Fntb^{fl/fl}$ ($n = 3$) mice under steady state. T$_{reg}$ cells were labelled with CTV and cultured with anti-CD3/28 antibodies plus IL-2 for 3 days. Flow cytometry analysis (left) and relative MFI (right) of PD-1 on CTV^{lo} cells. (**i**) Resting T$_{reg}$ cells were sorted from $Foxp3^{Cre}$ control and $Foxp3^{Cre}Rac1^{fl/fl}Rac2^{-/-}$ mice ($n = 4$ mice per genotype) under steady state, and cultured with anti-CD3/28 antibodies plus IL-2 for 3 days. Flow cytometry analysis (left) and relative MFI (right) of PD-1. (**j**) Foxp3-YFP$^+$CD4$^+$ cells were sorted from $Foxp3^{Cre}$ mice ($n = 5$) and stimulated with anti-CD3/28 antibodies plus IL-2 for 3 days, in the presence of vehicle control, simvastatin (2 mM), GGTI (5 mM), or two different AP-1 inhibitors [Sr11302 (30 mM) or T-5224 (120 mM)]. Flow cytometry analysis (upper) and relative MFI of PD-1 (lower). (**k**) Schematic of SREBP-driven metabolic and functional adaptation of T$_{reg}$ cells in the TME. SREBPs are activated in intratumoural T$_{reg}$ cells as a key driver of T$_{reg}$ cell functional specialization in the TME, which leads to suppression of effective antitumour immune responses and the reduced efficacy of immune checkpoint therapy. Mechanistically, SREBP-dependent *de novo* fatty acid synthesis and PD-1 signalling in T$_{reg}$ cells enforce T$_{reg}$ cell suppressive function in tumours. T$_{reg}$ cells show enhanced $Pdcd1$ expression in tumours, and this upregulation is dependent on SREBP-dependent mevalonate metabolism that further signals to Pggt1b-driven protein geranylgeranylation. PD-1 induction is required to repress overt IFN-γ production by T$_{reg}$ cells in response to TCR activation in the TME, suggesting that SREBP signalling supports intratumoural T$_{reg}$ cell functional fitness, in part, by preventing T$_{reg}$ cell fragility. Therefore, SREBP-dependent metabolic reprogramming enforces T$_{reg}$ cell functional specialization in tumours by coordinating lipid synthesis and inhibitory receptor signalling pathways. *$P <$ 0.05, **$P <$ 0.01, ***$P <$ 0.001, NS, not significant. Two-tailed unpaired Student's t-test (**a, b, g–i**) or one-way ANOVA (**c–f, j**). Data are mean ± s.e.m. in **a–j**. Data are compiled from three (**b–d, f, g**) or two (**a, e, h–j**) independent experiments. Values in control samples were set to 1 (**a–d, f–j**).

Supplementary Material

Refer to Web version on PubMed Central for supplementary material.

Acknowledgements

Data availability

Data generated in this study are included within the paper (and its supplementary information files) or are available from the corresponding author upon reasonable request. Microarray and scRNA-seq data that support the findings of this study have been deposited in the Gene Expression Omnibus (GEO) under the accession number GSE149573. Source data are provided with this paper.

REFERENCES

1. Savage PA, Klawon DEJ & Miller CH Regulatory T Cell Development. Annu Rev Immunol 38, 421–453, doi:10.1146/annurev-immunol-100219-020937 (2020). [PubMed: 31990619]

2. Sharma P, Hu-Lieskovan S, Wargo JA & Ribas A Primary, Adaptive, and Acquired Resistance to Cancer Immunotherapy. Cell 168, 707–723, doi:10.1016/j.cell.2017.01.017 (2017). [PubMed: 28187290]

3. Geltink RIK, Kyle RL & Pearce EL Unraveling the Complex Interplay Between T Cell Metabolism and Function. Annu Rev Immunol 36, 461–488, doi:10.1146/annurev-immunol-042617-053019 (2018). [PubMed: 29677474]

4. Chapman NM, Boothby MR & Chi H Metabolic coordination of T cell quiescence and activation. Nat Rev Immunol 20, 55–70, doi:10.1038/s41577-019-0203-y (2020). [PubMed: 31406325]

5. Newton R, Priyadharshini B & Turka LA Immunometabolism of regulatory T cells. Nat Immunol 17, 618–625, doi:10.1038/ni.3466 (2016). [PubMed: 27196520]

6. Horton JD, Goldstein JL & Brown MS SREBPs: activators of the complete program of cholesterol and fatty acid synthesis in the liver. J Clin Invest 109, 1125–1131, doi:10.1172/JCI15593 (2002). [PubMed: 11994399]

7. Sawant DV et al. Adaptive plasticity of IL-10(+) and IL-35(+) Treg cells cooperatively promotes tumor T cell exhaustion. Nat Immunol 20, 724–735, doi:10.1038/s41590-019-0346-9 (2019). [PubMed: 30936494]

8. Miragaia RJ et al. Single-Cell Transcriptomics of Regulatory T Cells Reveals Trajectories of Tissue Adaptation. Immunity 50, 493–504 e497, doi:10.1016/j.immuni.2019.01.001 (2019). [PubMed: 30737144]

9. Azizi E et al. Single-Cell Map of Diverse Immune Phenotypes in the Breast Tumor Microenvironment. Cell 174, 1293–1308 e1236, doi:10.1016/j.cell.2018.05.060 (2018). [PubMed: 29961579]

10. Cillo AR et al. Immune Landscape of Viral- and Carcinogen-Driven Head and Neck Cancer. Immunity 52, 183–199 e189, doi:10.1016/j.immuni.2019.11.014 (2020). [PubMed: 31924475]

11. van der Veeken J et al. Memory of Inflammation in Regulatory T Cells. Cell 166, 977–990, doi:10.1016/j.cell.2016.07.006 (2016). [PubMed: 27499023]

12. Pacella I et al. Fatty acid metabolism complements glycolysis in the selective regulatory T cell expansion during tumor growth. Proc Natl Acad Sci U S A 115, E6546–E6555, doi:10.1073/pnas.1720113115 (2018). [PubMed: 29941600]

13. Yang K et al. Homeostatic control of metabolic and functional fitness of Treg cells by LKB1 signalling. Nature 548, 602–606, doi:10.1038/nature23665 (2017). [PubMed: 28847007]

14. Rubtsov YP et al. Stability of the regulatory T cell lineage in vivo. Science 329, 1667–1671, doi:10.1126/science.1191996 (2010). [PubMed: 20929851]

15. Curran MA, Montalvo W, Yagita H & Allison JP PD-1 and CTLA-4 combination blockade expands infiltrating T cells and reduces regulatory T and myeloid cells within B16 melanoma tumors. Proc Natl Acad Sci U S A 107, 4275–4280, doi:10.1073/pnas.0915174107 (2010). [PubMed: 20160101]

16. Shi H et al. Amino Acids License Kinase mTORC1 Activity and Treg Cell Function via Small G Proteins Rag and Rheb. Immunity 51, 1012–1027 e1017, doi:10.1016/j.immuni.2019.10.001 (2019). [PubMed: 31668641]

17. DuPage M et al. The chromatin-modifying enzyme Ezh2 is critical for the maintenance of regulatory T cell identity after activation. Immunity 42, 227–238, doi:10.1016/j.immuni.2015.01.007 (2015). [PubMed: 25680271]

18. Kidani Y et al. Sterol regulatory element-binding proteins are essential for the metabolic programming of effector T cells and adaptive immunity. Nat Immunol 14, 489–499, doi:10.1038/ni.2570 (2013). [PubMed: 23563690]

19. Shi H et al. Hippo Kinases Mst1 and Mst2 Sense and Amplify IL-2R-STAT5 Signaling in Regulatory T Cells to Establish Stable Regulatory Activity. Immunity 49, 899–914 e896, doi:10.1016/j.immuni.2018.10.010 (2018). [PubMed: 30413360]

20. Boyman O, Kovar M, Rubinstein MP, Surh CD & Sprent J Selective stimulation of T cell subsets with antibody-cytokine immune complexes. Science 311, 1924–1927, doi:10.1126/science.1122927 (2006). [PubMed: 16484453]

21. Zeng H et al. mTORC1 couples immune signals and metabolic programming to establish T(reg)-cell function. Nature 499, 485–490, doi:10.1038/nature12297 (2013). [PubMed: 23812589]

22. Wang H et al. CD36-mediated metabolic adaptation supports regulatory T cell survival and function in tumors. Nat Immunol 21, 298–308, doi:10.1038/s41590-019-0589-5 (2020). [PubMed: 32066953]

23. Li MO & Rudensky AY T cell receptor signalling in the control of regulatory T cell differentiation and function. Nat Rev Immunol 16, 220–233, doi:10.1038/nri.2016.26 (2016). [PubMed: 27026074]

24. Wei J et al. Autophagy enforces functional integrity of regulatory T cells by coupling environmental cues and metabolic homeostasis. Nat Immunol 17, 277–285, doi:10.1038/ni.3365 (2016). [PubMed: 26808230]

25. Overacre-Delgoffe AE et al. Interferon-gamma Drives Treg Fragility to Promote Anti-tumor Immunity. Cell 169, 1130–1141 e1111, doi:10.1016/j.cell.2017.05.005 (2017). [PubMed: 28552348]

26. Di Pilato M et al. Targeting the CBM complex causes Treg cells to prime tumours for immune checkpoint therapy. Nature 570, 112–116, doi:10.1038/s41586-019-1215-2 (2019). [PubMed: 31092922]

27. Boehm U, Klamp T, Groot M & Howard JC Cellular responses to interferon-gamma. Annu Rev Immunol 15, 749–795, doi:10.1146/annurev.immunol.15.1.749 (1997). [PubMed: 9143706]

28. Lacher SM et al. HMG-CoA reductase promotes protein prenylation and therefore is indispensible for T-cell survival. Cell Death Dis 8, e2824, doi:10.1038/cddis.2017.221 (2017). [PubMed: 28542128]

29. Levine AG, Arvey A, Jin W & Rudensky AY Continuous requirement for the TCR in regulatory T cell function. Nat Immunol 15, 1070–1078, doi:10.1038/ni.3004 (2014). [PubMed: 25263123]

30. Vahl JC et al. Continuous T cell receptor signals maintain a functional regulatory T cell pool. Immunity 41, 722–736, doi:10.1016/j.immuni.2014.10.012 (2014). [PubMed: 25464853]

31. Kumagai S et al. The PD-1 expression balance between effector and regulatory T cells predicts the clinical efficacy of PD-1 blockade therapies. Nat Immunol 21, 1346–1358, doi:10.1038/s41590-020-0769-3 (2020). [PubMed: 32868929]

32. Moran AE et al. T cell receptor signal strength in Treg and iNKT cell development demonstrated by a novel fluorescent reporter mouse. J Exp Med 208, 1279–1289, doi:10.1084/jem.20110308 (2011). [PubMed: 21606508]

33. Wang M & Casey PJ Protein prenylation: unique fats make their mark on biology. Nat Rev Mol Cell Biol 17, 110–122, doi:10.1038/nrm.2015.11 (2016). [PubMed: 26790532]

34. Su W et al. Protein Prenylation Drives Discrete Signaling Programs for the Differentiation and Maintenance of Effector Treg Cells. Cell Metab, doi:10.1016/j.cmet.2020.10.022 (2020).

35. Xiao G, Deng A, Liu H, Ge G & Liu X Activator protein 1 suppresses antitumor T-cell function via the induction of programmed death 1. Proc Natl Acad Sci U S A 109, 15419–15424, doi:10.1073/pnas.1206370109 (2012). [PubMed: 22949674]

36. Lucca LE & Dominguez-Villar M Modulation of regulatory T cell function and stability by co-inhibitory receptors. Nat Rev Immunol, doi:10.1038/s41577-020-0296-3 (2020).

37. Liu C et al. Treg Cells Promote the SREBP1-Dependent Metabolic Fitness of Tumor-Promoting Macrophages via Repression of CD8(+) T Cell-Derived Interferon-gamma. Immunity 51, 381–397 e386, doi:10.1016/j.immuni.2019.06.017 (2019). [PubMed: 31350177]

38. Brovkovych V et al. Fatostatin induces pro- and anti-apoptotic lipid accumulation in breast cancer. Oncogenesis 7, 66, doi:10.1038/s41389-018-0076-0 (2018). [PubMed: 30140005]

REFERENCES

39. Rubtsov YP et al. Regulatory T cell-derived interleukin-10 limits inflammation at environmental interfaces. Immunity 28, 546–558, doi:Doi 10.1016/J.Immuni.2008.02.017 (2008). [PubMed: 18387831]

40. Khan OM et al. Geranylgeranyltransferase type I (GGTase-I) deficiency hyperactivates macrophages and induces erosive arthritis in mice. J Clin Invest 121, 628–639, doi:10.1172/JCI43758 (2011). [PubMed: 21266780]

41. Liu M et al. Targeting the protein prenyltransferases efficiently reduces tumor development in mice with K-RAS-induced lung cancer. Proc Natl Acad Sci U S A 107, 6471–6476, doi:10.1073/pnas.0908396107 (2010). [PubMed: 20308544]

42. Nagashima S et al. Liver-specific deletion of 3-hydroxy-3-methylglutaryl coenzyme A reductase causes hepatic steatosis and death. Arterioscler Thromb Vasc Biol 32, 1824–1831, doi:10.1161/ATVBAHA.111.240754 (2012). [PubMed: 22701022]

43. Wei J et al. Targeting REGNASE-1 programs long-lived effector T cells for cancer therapy. Nature 576, 471–476, doi:10.1038/s41586-019-1821-z (2019). [PubMed: 31827283]

44. Karmaus PWF et al. Metabolic heterogeneity underlies reciprocal fates of TH17 cell stemness and plasticity. Nature 565, 101–105, doi:10.1038/s41586-018-0806-7 (2019). [PubMed: 30568299]

45. Liu G et al. The receptor S1P1 overrides regulatory T cell-mediated immune suppression through Akt-mTOR. Nat Immunol 10, 769–777, doi:10.1038/ni.1743 (2009). [PubMed: 19483717]

46. Subramanian A et al. Gene set enrichment analysis: a knowledge-based approach for interpreting genome-wide expression profiles. Proc Natl Acad Sci U S A 102, 15545–15550, doi:10.1073/pnas.0506580102 (2005). [PubMed: 16199517]

47. Horton JD et al. Combined analysis of oligonucleotide microarray data from transgenic and knockout mice identifies direct SREBP target genes. Proc Natl Acad Sci U S A 100, 12027–12032, doi:10.1073/pnas.1534923100 (2003). [PubMed: 14512514]

48. Butler A, Hoffman P, Smibert P, Papalexi E & Satija R Integrating single-cell transcriptomic data across different conditions, technologies, and species. Nat Biotechnol 36, 411–420, doi:10.1038/nbt.4096 (2018). [PubMed: 29608179]

49. McInnes L, Healy J & Melville J UMAP: uniform manifold approximation and projection for dimension reduction. Preprint at https://arxiv.org/abs/1802.03426 (2018).

50. Folch J, Lees M & Sloane Stanley GH A simple method for the isolation and purification of total lipides from animal tissues. J Biol Chem 226, 497–509 (1957). [PubMed: 13428781]

51. Buescher JM et al. A roadmap for interpreting (13)C metabolite labeling patterns from cells. Curr Opin Biotechnol 34, 189–201, doi:10.1016/j.copbio.2015.02.003 (2015). [PubMed: 25731751]
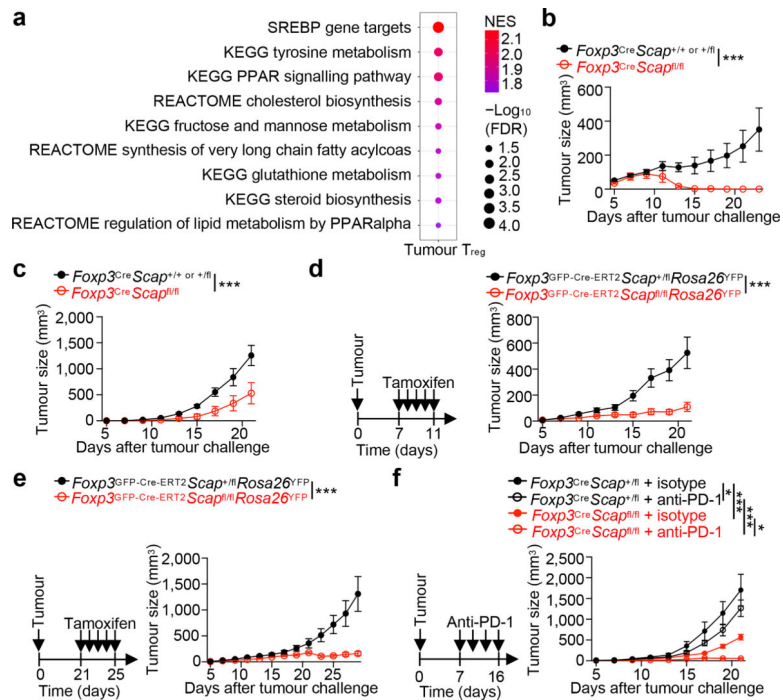
Figure 1. T_reg cells upregulate SREBP signalling and require SCAP/SREBP activity for their functional adaptation in tumours.

(**a**) List of the enriched cell metabolism-related pathways in intratumoural T_reg cells compared to those from PLNs ($n = 4$ per group) from B16 melanoma tumour-bearing mice. (**b**, **c**) $Foxp3^{Cre}Scap^{+/+ \text{ or } +/fl}$ ($n = 6$) and $Foxp3^{Cre}Scap^{fl/fl}$ ($n = 5$) mice were inoculated with MC38 cells (**b**) or B16 cells (**c**), and tumour growth was measured. (**d**, **e**) $Foxp3^{GFP-Cre-ERT2}Scap^{+/fl}Rosa26^{YFP}$ (**d**, $n = 6$; **e**, $n = 6$) and $Foxp3^{GFP-Cre-ERT2}Scap^{fl/fl}Rosa26^{YFP}$ (**d**, $n = 6$; **e**, $n = 7$) mice were injected with MC38 cells on day 0 and treated with tamoxifen on days 7–11 (**d**, left) or days 21–25 (**e**, left). Tumour growth (right) was measured. (**f**) $Foxp3^{Cre}Scap^{+/fl}$ and $Foxp3^{Cre}Scap^{fl/fl}$ mice were inoculated with B16 cells on day 0 and treated with either anti-PD-1 or isotype control antibody on days 7, 10, 13, and 16 (left). Tumour growth (right) was measured ($n = 7$, $Foxp3^{Cre}Scap^{+/fl}$ + isotype; $n = 6$, $Foxp3^{Cre}Scap^{+/fl}$ + anti-PD-1; $n = 5$, $Foxp3^{Cre}Scap^{flfl}$ + isotype; $n = 5$, $Foxp3^{Cre}Scap^{fl/fl}$ + anti-PD-1). $*P < 0.05$, $***P < 0.001$. Two-way ANOVA (**b**–**f**). Data are mean ± s.e.m. in **b**–**f**. Data are representative of five (**c**) or two (**b**, **d**, **e**) independent experiments.
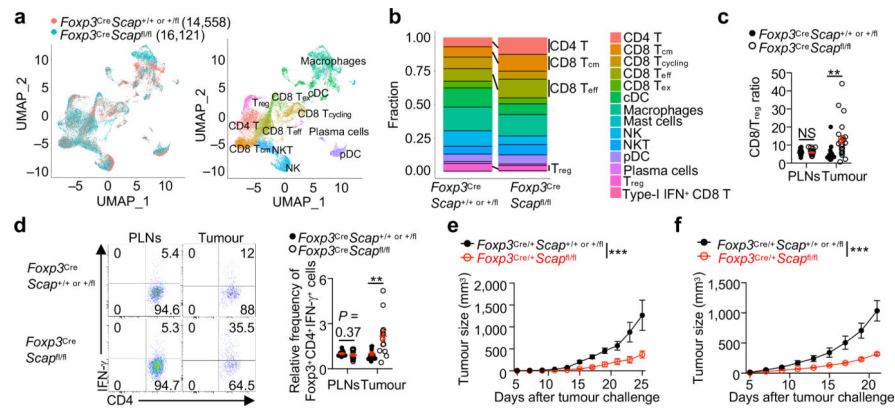
Figure 2. SREBPs maintain T_reg cell functional fitness in the TME.

(**a**, **b**) $Foxp3^{Cre}Scap^{+/+ \text{ or } +/fl}$ and $Foxp3^{Cre}Scap^{fl/fl}$ mice ($n = 2$ mice per genotype) were inoculated with B16 cells and CD45$^+$ tumour-infiltrating lymphocytes (TILs) were isolated on day 19, followed by scRNA-seq analysis. (**a**) UMAP embeddings of merged scRNA-seq showing distribution of CD45$^+$ TILs (left) and immune cell subsets (right). (**b**) Proportions of immune cell subsets of scRNA-seq. (**c**) $Foxp3^{Cre}Scap^{+/+ \text{ or } +/fl}$ ($n = 18$) and $Foxp3^{Cre}Scap^{fl/fl}$ ($n = 23$) mice were inoculated with B16 cells and sacrificed on day 19 for the quantification of CD8/T_reg cell ratio in PLNs and tumours. (**d**) $Foxp3^{Cre}Scap^{+/+ \text{ or } +/fl}$ control ($n = 11$) and $Foxp3^{Cre}Scap^{fl/fl}$ ($n = 14$) mice were inoculated with B16 cells, and flow cytometry analysis of IFN-γ expression in Foxp3$^+$CD4$^+$ T cells (left panel) and relative frequency (right panel; values in control samples were set to 1) of IFN-γ in Foxp3$^+$CD4$^+$ T cells from PLNs and tumours. (**e**) B16 cells were inoculated into $Foxp3^{Cre/+}Scap^{+/+ \text{ or } +/fl}$ and $Foxp3^{Cre/+}Scap^{fl/fl}$ bone marrow chimeras ($n = 4$ mice per genotype). Tumour growth was measured. (**f**) MC38 cells were inoculated into $Foxp3^{Cre/+}Scap^{+/+ \text{ or } +/fl}$ and $Foxp3^{Cre/+}Scap^{fl/fl}$ mosaic mice ($n = 7$ mice per genotype). Tumour growth was measured. **$P < 0.01$, ***$P < 0.001$, NS, not significant. Two-tailed unpaired Student's t-test (**c**, **d**) or two-way ANOVA (**e**, **f**). Data are mean ± s.e.m. in **c**–**f**. Data are representative of two (**e**, **f**), or compiled from four (**c**) or two (**d**) independent experiments.
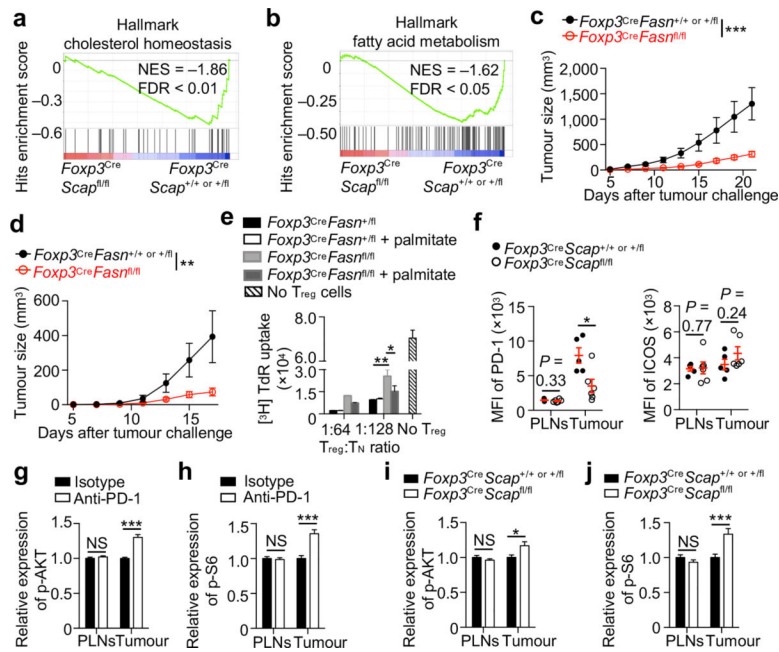
Figure 3. SREBPs orchestrate intratumoural T$_{reg}$ cell function through coordinating *de novo* lipid synthesis and PD-1 expression.

(**a**, **b**) Enrichment plots showing downregulated cholesterol homeostasis (**a**) and fatty acid metabolism (**b**) in intratumoural T$_{reg}$ cells from *Foxp3*^{Cre}*Scap*$^{+/+ \text{ or } +/fl}$ ($n = 4$) mice versus *Foxp3*^{Cre}*Scap*$^{fl/fl}$ ($n = 3$) mice. (**c**, **d**) *Foxp3*^{Cre}*Fasn*$^{+/+ \text{ or } +/fl}$ (**c**, $n = 6$; **d**, $n = 5$) and *Foxp3*^{Cre}*Fasn*$^{fl/fl}$ (**c**, $n = 7$; **d**, $n = 5$) mice were inoculated with MC38 (**c**) or B16 cells (**d**). Tumour growth was measured. (**e**) Control and FASN-deficient T$_{reg}$ cells were activated in the presence or absence of palmitate, followed by *in vitro* suppression assay. T$_N$, naïve CD4$^+$ T cells. (**f**) PD-1 (left) and ICOS (right) levels on T$_{reg}$ cells in PLNs and tumours from B16 melanoma-bearing *Foxp3*^{Cre}*Scap*$^{+/+ \text{ or } +/fl}$ ($n = 5$) and *Foxp3*^{Cre}*Scap*$^{fl/fl}$ ($n = 6$) mice on day 19. (**g**, **h**) MC38 tumour-bearing mice were treated with anti-PD-1 or isotype control antibody on days 7, 10, and 13 ($n = 20$ per group). Quantified p-AKT (**g**) and p-S6 (**h**) MFIs in Foxp3$^+$CD4$^+$ T cells in PLNs and tumours on day 14. (**i**, **j**) *Foxp3*^{Cre}*Scap*$^{+/+ \text{ or } +/fl}$ control and *Foxp3*^{Cre}*Scap*$^{fl/fl}$ mice were inoculated with B16 cells. Quantified p-AKT (**i**) and p-S6 (**j**) MFIs in intratumoural T$_{reg}$ cells in PLNs ($n = 17$ per genotype) and tumours ($n = 14$, *Foxp3*^{Cre}*Scap*$^{+/+ \text{ or } +/fl}$ mice; $n = 15$, *Foxp3*^{Cre}*Scap*$^{fl/fl}$ mice) on day 14. *$P < 0.05$, **$P < 0.01$, ***$P < 0.001$, NS, not significant. Two-tailed unpaired Student's *t*-test (**f**–**j**) or one-way ANOVA (**e**) or two-way ANOVA (**c**, **d**). Data are mean ± s.e.m. in **c**–**i**. Data are representative of three (**d**) or two (**c**, **e**, **f**), or compiled from two (**g**–**j**) independent experiments. Values in control samples were set to 1 (**g**–**j**).
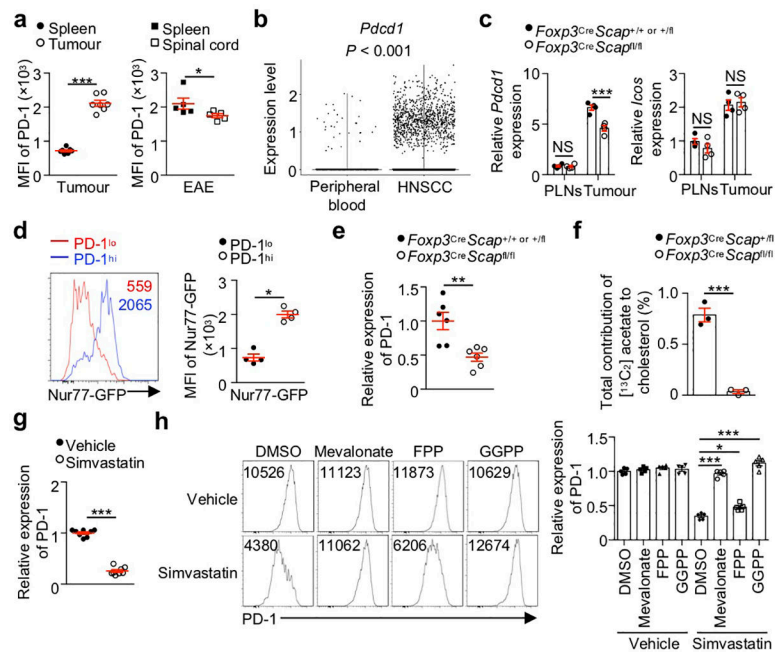
Figure 4. Mevalonate metabolism-driven protein geranylgeranylation enforces T_{reg} cell PD-1 upregulation.

(**a**) PD-1 expression on T_{reg} cells from MC38 tumour-bearing mice ($n = 7$; day 21) or MOG-induced EAE mice ($n = 5$; day 16). (**b**) Violin plot of *Pdcd1* expression in T_{reg} cells from scRNA-seq dataset of human patients with HNSCC. (**c**) Real-time PCR analysis of relative *Pdcd1* and *Icos* mRNA expression in T_{reg} cells from B16 melanoma-bearing *Foxp3*^{Cre}*Scap*$^{+/+ \text{ or } +/fl}$ and *Foxp3*^{Cre}*Scap*$^{fl/fl}$ mice ($n = 4$ samples per genotype). (**d**) Flow cytometry analysis (left) and quantification (right) of Nur77-GFP expression in PD-1^{hi} and PD-1^{lo} T_{reg} cells in B16 melanoma ($n = 4$). (**e**) Relative PD-1 expression on *Foxp3*^{Cre}*Scap*$^{+/+ \text{ or } +/fl}$ or *Foxp3*^{Cre}*Scap*$^{fl/fl}$ T_{reg} cells ($n = 6$ samples per genotype) that were stimulated by anti-CD3/28 antibodies plus IL-2 for 3 days. (**f**) Incorporation of ^{13}C into cholesterol in control and SCAP-deficient T_{reg} cells ($n = 3$ samples per genotype) that were stimulated with anti-CD3/28 antibodies plus IL-2 in the presence of [$^{13}C_2$]-sodium acetate for 2 days. (**g**) Relative PD-1 expression on vehicle- or simvastatin-treated T_{reg} cells that were stimulated with anti-CD3/28 antibodies plus IL-2 for 3 days ($n = 8$). (**h**) Flow cytometry analysis (left) and quantification (right) of relative PD-1 expression on vehicle- or simvastatin-treated CellTrace Violet (CTV)^{lo} T_{reg} cells that were stimulated with anti-CD3/28 antibodies plus IL-2 for 3 days in the presence of mevalonate, FPP, GGPP, or DMSO ($n = 5$). $*P < 0.05$, $**P < 0.01$, $***P < 0.001$, NS, not significant. Two-tailed unpaired Student's *t*-test (**a**, **c**–**g**) or one-way ANOVA (**h**). Data are mean ± s.e.m. in **a**–**h**. Data are representative of two (**a**), or compiled from three (**g**) or two (**e**, **h**) independent experiments.